Summer 2014

# Preparation & characterization of high purity Cu2 ZnSn(SxSe1-x)4 nanoparticles

Bethlehem G. Negash
*Purdue University*

Graduate School ETD Form 9
(Revised 01/14)

# PURDUE UNIVERSITY
## GRADUATE SCHOOL
## Thesis/Dissertation Acceptance

This is to certify that the thesis/dissertation prepared

By Bethlehem Negash

Entitled
Preparation & Characterization of High Purity Cu2ZnSn(SxSe1-x)4 Nanoparticles

For the degree of Master of Science

Is approved by the final examining committee:

Dr. Rakesh Agrawal

Dr. Michael Harris

Dr. Bryan Boudouris

To the best of my knowledge and as understood by the student in the *Thesis/Dissertation Agreement, Publication Delay, and Certification/Disclaimer (Graduate School Form 32)*, this thesis/dissertation adheres to the provisions of Purdue University's "Policy on Integrity in Research" and the use of copyrighted material.

Approved by Major Professor(s): Rakesh Agrawal

Approved by: Dr. John Morgan 07/10/2014

Head of the Department Graduate Program Date

# PREPARATION & CHARACTERIZATION OF HIGH PURITY $Cu_2ZnSn(S_xSe_{1-x})_4$ NANOPARTICLES

A Thesis

Submitted to the Faculty

of

Purdue University

by

Bethlehem G. Negash

In Partial Fulfillment of the

Requirements for the Degree

of

Master of Science in Chemical Engineering

August 2014

Purdue University

West Lafayette, Indiana

To my family and friends

# ACKNOWLEDGEMENTS

I would like to express my deep gratitude to Professor Rakesh Agrawal, my research supervisor, for his patient guidance and useful critiques of this research work. Dr. Agrawal, among many things, has thought me to never be satisfied with my work but to always look for improvements and aspire for more. Dr. Agrawal's passion and enthusiasm for research remains unmatched in my eyes. His creativity and ability to bring together knowledge and expertise from various disciplines is inspiring. I would also like to thank my thesis committee members, Dr. Bryan Boudouris and Dr. Michael Harris for their valuable input and suggestions towards improving this research

I wish to acknowledge several people for contribution to this work; thanks to members of the Solar Energy Research Group for their teamwork and support. A special thanks to Dr. Bryce Walker, who severed as my mentor during my first summer internship in the Solar Lab, and who continued to mentor me throughout my graduate school career. His thoughtful ideas and input were vital for the progress of this research. Thanks to Caleb Miskin, for working closely with me on data acquisition and analysis as we prepare on publishing this work. I would also like to extend my deepest gratitude to all members of the Solar Lab for their help with data acquisition and analysis throughout my stay at Purdue.

.

I would like to thank our collaborators in the Department of Chemistry; thanks to Dr. Karl Wood for conducting mass spectrometry analysis and valuable input in understanding fragmentation patterns of amines in various mass spectrometry systems. Thanks to John Degenstein for his contributive discussions during mass spec data analysis and for serving as an excellent bridge for future collaboration with Dr. Hilkka Kenttämaa's research group.

Finally, I would like to extend a very special thanks to my family and friends for their love and support throughout this process.

# TABLE OF CONTENTS

Page

# LIST OF TABLES

# LIST OF FIGURES

Figure Page

# LIST OF ABBREVIATIONS

CBD: Chemical Bath Deposition

CIGSe: Copper Indium Gallium Selenide ($Cu_2(In,Ga)Se_2$)

CZTS: Copper Zinc Tin Sulfide ($Cu_2ZnSnS_4$)

CZTSe: Copper Zinc Tin Sulfide ($Cu_2ZnSnSe_4$)

CZTSSe: CZTS: Copper Zinc Tin Sulfoselenide ($Cu_2ZnSn(S_xSe_{1-x})_4$)

DFT: Density Functional Theory

EDS: Energy Dispersive X-ray Spectroscopy

ESI-MS: Electrospray Ionization Mass Spectrometry

FTIR: Fourier Transform Infrared

GC-MS: Gas Chromatography Mass Spectrometry

GDP: Gross Domestic Product

KS: Kesterite

LED: Light Emitting Diode

NMR: Nuclear Magnetic Resonance

OLA: Oleylamine

PCE: Power Conversion Efficiency

PD-KS: Partially Disordered Kesterite

PMCA: Primitive Mixed Cu-Au Structure

PVD: Physical Vapor Deposition

(P)XRD: Powder X-ray Diffraction

SEM-EDS: Scanning Electron Microscopy- Energy Dispersive X-ray Spectroscopy

ST: Stannite

TOPO: Tri-n-octylphosphine Oxide

Voc: Open Circuit Voltage

# ABSTRACT

Negash, Bethlehem G. M.S.Ch.E., Purdue University, August 2014. Preparation & Characterization of High Purity $Cu_2ZnSn(S_xSe_{1-x})_4$ Nanoparticles. Major Professor: Rakesh Agrawal.

Research in thin film solar cells applies novel techniques to synthesize cost effective and highly efficient absorber materials in order to generate electricity directly from solar energy. Of these materials, devices made using copper zinc tin sulfoselenide ($Cu_2ZnSn(S_xSe_{1-x})_4$) nanoparticles have shown great promise in solar cell applications due to optimal material properties as well as low cost & relative abundance of materials.[1,2] Sulfoselenide nanoparticles have also a broader impact in other industries including electronics[3], LED[4], and biomedical research[5]. Of the many routes of manufacturing these class of nanoparticles, colloidal synthesis of $Cu_2ZnSn(S_xSe_{1-x})_4$ offers a scalable, low cost and high-throughput route for manufacturing materials for high efficiency thin-film solar cells. Recently, hydrazine processed $Cu_2ZnSn(S_xSe_{1-x})_4$ devices have reached a record power conversion efficiency (PCE) of 12.6%, much higher than the 9.6% reported for physical vapor deposition (PVD) systems.[6,7]

Despite high efficiencies, wet synthesis of nanoparticles, is made more complicated in multi-element, quaternary and quinary systems such as copper zinc tin sulfoselenide (CZTSSe)One major disadvantage in these systems is growth of the desired quaternary or quinary phase in competition with unwanted binary and ternary phases, which have low energy of formation.[8,9] Moreover, various reaction parameters such as reaction time, temperature, and choice of ligand also affect chemical as well as physical properties of resulting nanoparticles.

Understanding formation mechanisms of the particles is necessary in order to address some of these challenges in wet synthesis of CZTSSe nanoparticles. In this study, we investigate synthesis conditions as well as reaction parameters necessary to yield high purity $Cu_2ZnSn(S_xSe_{1-x})_4$ nanoparticles as well as attempt to understand the growth mechanism of these nanoparticles. This was achieved by manipulating anion precursor preparation routes as well as order in which precursors are introduced into a reaction system. We report a new solution based sulfoselenide preparation route which has been used to synthesize high purity $Cu_2ZnSn(S_xSe_{1-x})_4$ nanoparticles. Uniform phase $Cu_2ZnSn(S_xSe_{1-x})_4$ nanoparticles were successfully synthesized over a wide range of varying chalcogen ratios. It was found that anion precursor solution plays a key role in determining the morphology & phase purity of the final nanoparticles, as observed from X-ray Diffraction (XRD) and Raman spectroscopy. A uniform sulfoselenide solution is needed to produce high purity $Cu_2ZnSn(S_xSe_{1-x})_4$ nanoparticles with narrow phase distribution. Moreover, the relative reactivity of each anion must be balanced in order to yield uniform phase nanoparticles. The findings of this study as well as the reported mixed chalcogen precursor preparation route can be applied in various industries, including photovoltaics to produce uniform phase, solution processed sulfoselenide nanoparticles.

# CHAPTER 1. INTRODUCTION & THESIS OUTLINE

## 1.1 Significance & Purpose of Study

Copper zinc tin sulfoselenide, $Cu_2ZnSn(S_xSe_{1-x})$, (CZTSSe) nanoparticles have been an attractive absorber material for thin-film solar cells due to their optimal band gap of ~1.5 eV and high absorption coefficient, $>10^{-4}$ $cm^{-1}$.[1,2,10] Solution based CZTSSe nanoparticles have been processed through various routes including electrodeposition[11,12] , hydrazine-based slurry coating[6,13,14], molecular precursor route[15] as well as solvent dispersed nanoparticle deposition.[16–20] Solution based synthesis of CZTSSe particles has received attention recently as it provides a less energy intensive & easily scalable route for manufacturing materials for solar cells.[14,17,21] Power conversion efficiency (PCE) for solution processed CZTSSe devices are also on the rise, reaching 12.6 %, for hydrazine processed systems[6] and 9.8% (active area) using less toxic wet synthesis routes.[20] Although these efficiencies are much lower than the more advanced copper indium gallium diselenide, $(Cu_2(In,Ga)Se_2)$, (CIGSe) systems which have reached PCE >20%[22], PCE for solution processed CZTSSe devices has shown promising progress, showing increase from 11.1% to 12.6% in one year. Most of this progress in efficiency can be attributed to improvement in coating uniformity and film structure as well as optimization of the transparent conducting oxide (TCO) and cadmium sulfide (CdS) layers.[6,14] Despite its advantages, colloidal synthesis of $Cu_2ZnSn(S_xSe_{1-x})_4$ nanoparticles has drawbacks including instability of material during film processing as well as lack of understanding of the growth mechanism of particles.[23,24]In addition, nanoparticles prepared using this route are prone to impurity formation due to the low energies of formation of binary and ternary phases.[8,9]

These undesirable phases may limit device performance by altering bulk properties of the absorber layer and serving as potential trap sites for charge carriers. One way to study growth mechanism of kesterite phase copper zinc tin sulfide, $Cu_2ZnSnS_4$, (CZTS) or copper zinc tin selenide, $Cu_2ZnSnSe_4$, (CZTSe) nanoparticles would be to synthesize mixed chalcogen particles with controlled ratios of sulfur and selenium. In addition to offering insight into structural evolution of kesterite phase nanoparticles, mixed chalcogen nanoparticles also offer the unique advantage of tuning optical properties of the material.[25–27]

Fabrication of devices from solution processed CZTS nanoparticles involves high temperature heat treatment of coated films under selenium vapor in order to induce grain growth through reactive sintering.[16] Large grains have been shown to reduce the number of grain boundaries which charge carriers have to overcome before being collected at the contacts. This annealing step, although crucial, does not give much control over the elemental composition of the final film. In order to insure that the compositional uniformity of the particles is insured at the atomic levels, mixed chalcogen CZTSSe nanoparticles can be prepared using wet synthesis and processed to produce solar devices. The challenge here lies in balancing the incorporation of sulfur and selenium in the reaction system as well as suppressing the formation of separate CZTS and CZTSe phases in competition with the desired CZTSSe phase.[28]

This study aims to address some of these aforementioned challenges and gain insight into synthesis routes which are needed to yield high purity kesterite phase $Cu_2ZnSn(S_xSe_{1-x})$ nanoparticles. To this effect, mixed chalcogen CZTSSe nanoparticles were synthesized using anion precursors prepared and/or introduced into the reaction system in different ways. Anion precursor solution was found to play an important role in determining final structure of synthesized nanoparticles. Growth mechanism of kesterite phase CZTSSe nanoparticles was also studied by introducing different concentrations sulfur or selenium to a hot solution containing CZTSe or CZTS nanoparticles, respectively. Results from this study show that CZTSe nanoparticles, once formed, are quite stable. Even after 5

hours of reaction time after a concentrated solution of sulfur was introduced to a hot solution containing CZTSe nanoparticles, (S:Se=2:1), the crystal structure of the CZTSe nanoparticles remained intact as confirmed from XRD. In the reverse experiment, where concentrated selenium solution was introduced into a hot solution containing CZTS nanoparticles, (S:Se=1:2), XRD analysis revealed a distinct CZTSe phase formation in the solution, which continues to grow with longer reaction times

## 1.2 Thesis Outline

This thesis highlights the preparation and characterization of high purity $Cu_2ZnSn(S_xSe_{1-x})_4$ nanoparticles. The role of anion precursor in structure of synthesized nanoparticles was also investigated.

Chapter 2 provides some background information about the need for renewable energy and solar energy as a viable source of energy for the future and provides. An overview of a solar device is given by highlighting major components of a solar cell and discussing physics of solar cells. As improvement in performance is the underlying goal of any research in photovoltaics, loss mechanisms of solar cells as well as the contribution of crystal structure of nanoparticles to these losses are also highlighted. The discussion is then geared into different class of inorganic semiconductors with much emphasis given to $I_2$-II-IV-$VI_4$ compound $Cu_2ZnSn(S_xSe_{1-x})_4$; with much emphasis given to various preparation and deposition techniques of these class of semiconductors. Finally, progress and challenges in colloidal synthesis of $Cu_2ZnSn(S_xSe_{1-x})_4$ nanoparticles is discussed in detail with much emphasis given to hot-injection method used to synthesize nanoparticles as well as synthesis conditions which affect growth evolution of nanoparticles.

Chapter 3 provides motivation and experimental details. It highlights key synthesis conditions and methods, including cation & anion precursor preparation routes used in this study as well as synthesis procedure of CZTSSe nanoparticles.

Chapter 4 presents the findings and discussion of this study. Synthesis and characterization of high purity CZTSSe nanoparticles is discussed first followed by a study in determining the role of anion precursor solution in the final crystal structure of synthesized nanoparticles. Finally, the reactivity of sulfur and selenium in these systems is investigated. Conclusions and suggestions for further work are provided in Chapter 5.

# CHAPTER 2. BACKGROUND

## 2.1 The Need for Renewable Energy

### 2.1.1. Current Energy Scenario

*Energy Crisis of 1973*

Interest in renewable energy appears to have skyrocketed over the last decade, with green movements being advertised in every sector. In U.S. history, the energy crisis of the 70s is notable in jumpstarting research in renewable energy. In 1973, an embargo on oil shipments placed by the Organization of Arab Petroleum Exporting Countries (OAPEC) on United States and other allied powers led to the infamous energy crises of the 70s. Although the restriction was removed within a year, the effects lingered for almost a decade with oil prices being raised from $3 a barrel to $12 a barrel.[29] The energy crisis was directly responsible for the birth of the Department of Energy in 1977 whose efforts towards lowering dependence on fossil fuels and developing alternate forms of energy are shaping U.S. energy consumption to this day.

*Future Energy Demands*

Future energy demands are calculated based on 'proven' reserves of oil, natural gas and coal. These are fossil fuel mines which can be excavated with current technology in a manner which is profitable. These calculations reveal that fossil fuels will be around for the next 100 years or more.[30] With increasing technologies, this number could go up to well more than the current estimate. So, if there isn't a risk of fossil fuel depletion in the immediate future, why is there a need to develop renewable sources of energy? Fossil fuels, although a concentrated form of energy, are devastating to the environment.

*Environmental Issues*

Carbon emissions from fossil fuel based sources of energy such as coal, natural gas and oil are major sources of pollution in the U.S. and the world at large. In the U.S. these sources of fuel account for 68% of electricity generation. Coal, a major source of electricity in the United States, accounted for 38% of total U.S. $CO_2$ emissions in 2011 and 37% in 2012.[31] After the Industrial Revolution in the 1950s, anthropogenic $CO_2$ emissions have skyrocketed and surpassed the rate of $CO_2$ reduction through natural sinks. These changes have resulted in major global climate change such as rise in sea levels, melting of ice caps, more occurrences of heat waves, more drought affected areas and other extreme climate.[32] Alternate sources of energy, such as solar energy, provide sustainable and low emission options to fossil fuels. Moreover, economic development across the world is an inevitable fate indicated by the annual percent increase in GDP for most countries around the world.[33] With the population of our planet continuing to grow, 1.2% annual increase, which is about 83 million a year[33] , and with the overall improvement of standard of life, alternate sources of energy are required to supply energy for an ever increasing demand.

### 2.1.2. Solar Energy

Solar energy is a reliable and consistent form of energy. Nearly $4 \times 10^{20}$ MW of power is generated by the sun every second. However, by the time the energy form the sun reaches the earth's atmosphere, this energy is diluted a great amount to about 1.37 KW power per square meter. This is further reduced to 1 $KW/m^2$ due to scattering, reflecting and absorption effects of the atmosphere.[34] Although there exists what seems to be a "limitless" supply of energy from the sun, the difficulty lies in harvesting this energy in a manner which is inexpensive and efficient. Thin film photovoltaics (PVs) are a promising technology in this aspect, especially for large scale application. PVs have no moving parts which makes their assembly and maintenance inexpensive. Moreover, the absorber layer in a PV device can be synthesized from low cost, earth abundant materials by using less energy intensive solution based techniques. Although, PV technology has shown a

great deal of potential, cost of production must drop down significantly for it to be competitive with existing sources of energy, such as fossil fuels.

## 2.2 Overview of a Solar Device

The general premise of a photovoltaic device is to collect energy from the sun and convert it directly to electricity. Figure 2.1 shows the basic set up of an inorganic photovoltaic device.

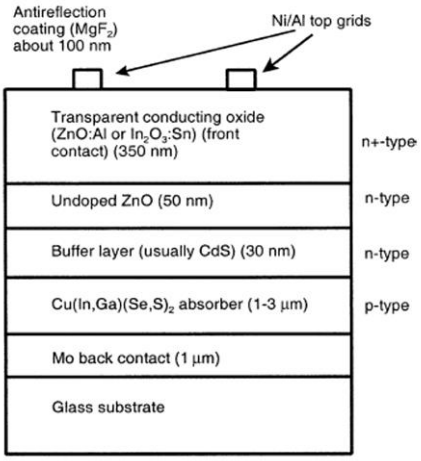


Figure 2.1 Components of a Typical Solar Cell[1] (Image not drawn to scale)

Figure 2.1 illustrates the components of a typical solar device. The device consists of a 1μm thick layer of molybdenum (Mo) sputtered onto a glass substrate; Mo serves as the back contact of the cell. Typically, a 1-3 μm thick (p-type) absorber layer (CIGSSe,CZTSSe) is deposited on a molybdenum coated soda-lime glass substrate. Generally, the film is then annealed at high temperatures (~500°C) under selenium vapor in order to induce grain growth and passivate grain boundaries. The p-n junction is completed by the deposition of a thin buffer layer (~50nm) of cadmium sulfide (CdS, n-type) over the p-type absorber layer via chemical bath deposition (CBD). Next, an intrinsic zinc oxide (i-ZnO) window layer and a highly conductive transparent conducting oxide, tin-doped indium oxide (ITO) layer are sputtered over the CdS layer. The device is completed by the thermal evaporation of Ni/Al metal, which serve as front contacts.[35]

[1] Image is courtesy of the Solar Energy Group

### 2.2.1. Band Gap

Solar energy is a form of electromagnetic radiation, having characteristics of both a wave and a particle. When a photon of light impacts a photovoltaic device, it causes electrons from atoms in the absorber layer to become excited from their bound state in the valence energy band to their free state in the conduction energy band. A free electron leaves behind what is referred to as a hole and designated with a positive charge. Both electrons and holes are referred to as charge carriers and are directly involved in conduction of electricity. The energy required to excite an electron from its bound state to its free state is called the band gap ($E_g$). A photon incident on a solar device must have energy equal to the band gap of that particular material in order to efficiently generate an electron-hole pair. A photon of lower energy is weakly absorbed by the material and is simply transmitted through it, while a photon of high energy strongly excites an electron causing it to thermalize back down, losing heat.[34]

### 2.2.2. p-n Junction

The p-n junction establishes the boundary of the built in potential difference. It consists of two semiconductor regions with opposite doping type. A negative-carrier (donor) dopant is an atom which can supply an extra electron in the material. In silicon, there are four valance electrons, which are part of bonds in the crystal. In n-type silicon, a dopant such as phosphorous is introduced. Phosphorous, having five valence electrons, supplies an electron to each of the four silicon bonds but also has an extra “free” electron. The opposite, a positive-carrier (acceptor) dopant has one fewer valence electron than the material, and provides electron vacancies (holes) in the crystal lattice. These holes act like free positive charges moving through the crystalline material. Boron, which has 3 valence electrons is typically used as an acceptor dopant in silicon.

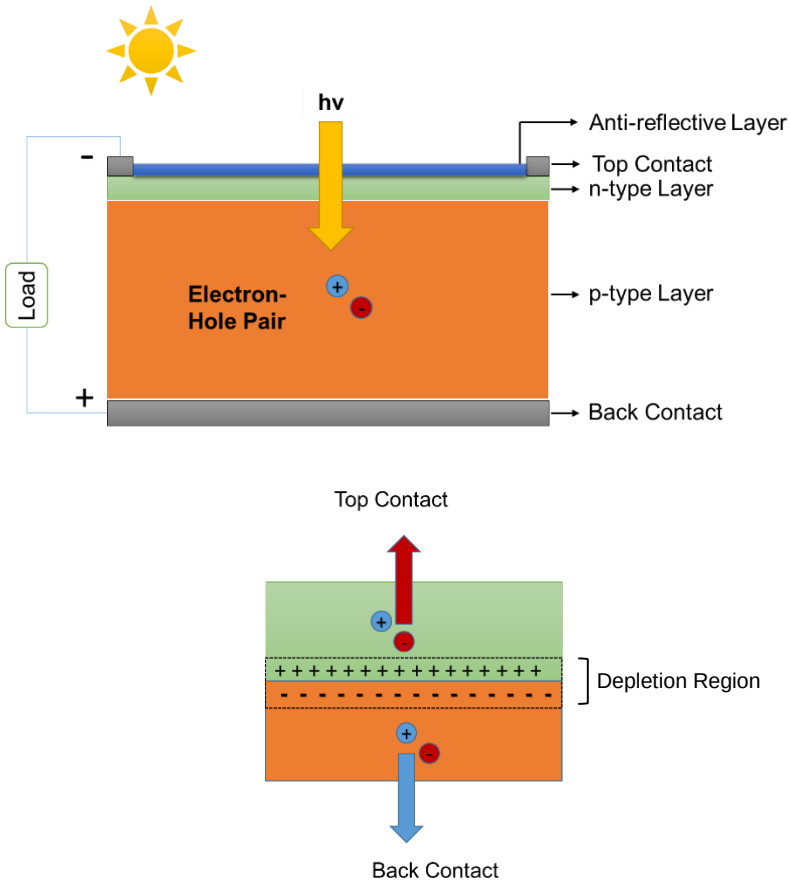


Figure 2.2 p-n Junction (Image not drawn to scale)

When a p-type and n-type material come together, a barrier is set up as a result of two opposing charges. Majority carriers (holes) from the p-type region flow towards the n-type region and vice versa until an equilibrium is established. This in turn creates a built in field at the junction, known as the depletion region, which prevents majority carries from further crossing sides at equilibrium. This potential difference in the cell is what is used to drive current flow and generate electricity.[34,36]

### 2.2.3. Loss Mechanisms

The first loss process occurs when a photon of light impacts a solar device. Incident light with energy below the band gap of the absorber material does not have enough energy to absorb an electron-hole pair; it passes through the material as if it were transparent. Light with energy above the band gap is strongly absorbed. For solar cell applications, this is not beneficial because the photon energy greater than the band gap is wasted as electrons quickly thermalize back down to the conduction band edge.[34,36,37]

Generation of an electron-hole pair by itself does not result in conduction. Free electrons in a solar cell are in a metastable state and in the absence of a built in potential barrier, they would simply thermalize back down from the conduction band and recombine with a hole in the valence band. Recombination is a type of loss mechanism and it limits the carrier lifetime and as a result the efficiency of a solar device. Types of recombination in solar cells include: 1) radiative recombination (band to band recombination), and 2) Shockley-Read-Hall recombination (recombination through defect sites).[34,36,37] Studies of intrinsic grain boundaries in CZTSe through first principle density functional theory (DFT) calculations have shown that grain boundaries create localized states within the band gap of a material, which act as Shockley-Read-Hall recombination sites.[38] In multi-element systems such as CZTSSe, defects in crystal lattice as a result of phase segregation and lattice mismatch could potentially serve as recombination sites and limit the performance in a solar cell.

## 2.3. Inorganic Solar Cells

The PV market share is dominated by multicrystalline Si (46%) and monocrytalline Si (38%). Thin film PVs only account for a small percentage of this market share.[39] This can be attributed to higher abundance of silicon, better optimization of silicon systems and simplicity of a single element system. Another class of PV materials, III-V compounds, such as gallium arsenide (GaAs), indium phosphide (InP), gallium antimonide (GaSb) are direct band gap materials which have near optimal band gap. High crystalline structures

of these materials have good carrier lifetimes and mobility which directly relates to carrier collection and efficiency. Cadmium telluride (CdTe), a II-VI thin film material, is a widely used inorganic PV due to its optimal band gap of 1.5 eV and high optical absorption.[40] The latter property allows this material to absorb a large amount of the incident radiation while short minority diffusion length of just a few microns allows for inexpensive material processing. CdTe has a disadvantage in that forming an ohmic contact with the substrate is difficult because its work function is higher than most metals.[39,40] I-III-VI compounds (Chalcopyrites), such as $CuIn_{1-x}Ga_xSe_2$ (CIGS), have also shown great promise with small area power conversion efficiency of greater than 20% achieved in lab.[22]

### 2.3.2. $I_2$-II-IV-$VI_4$ Compounds

This class of inorganic PV absorber materials has recently been studied due to near optimal band gap, low processing cost, and high absorption coefficient for photons with energies higher than the band gap.[39–41] Some methods of fabricating these materials include vacuum deposition, hydrazine based processing[6,13,14], solid state reaction of elemental powders[42], and pulsed laser deposition of quaternary nanoparticles.[43] A less energy intensive and high throughput process of synthesizing these nanoparticles is a solution based synthesis process. Solution processed CZTSSe devices have achieved PCE of 12.6% compared to 9.7% for PVD processes.[6,7]

One of the obvious disadvantages of solution based synthesis of $I_2$-II-IV-$VI_4$ compounds is the complexity of a quaternary system and the difficulty it presents to achieve monodispersed, single phase nanoparticles. Due to the complexity of these structures, there are various forms possible crystal structures which exists in the synthesized sample. These crystal structures are a function of variation in the packing mechanism of each individual atom.

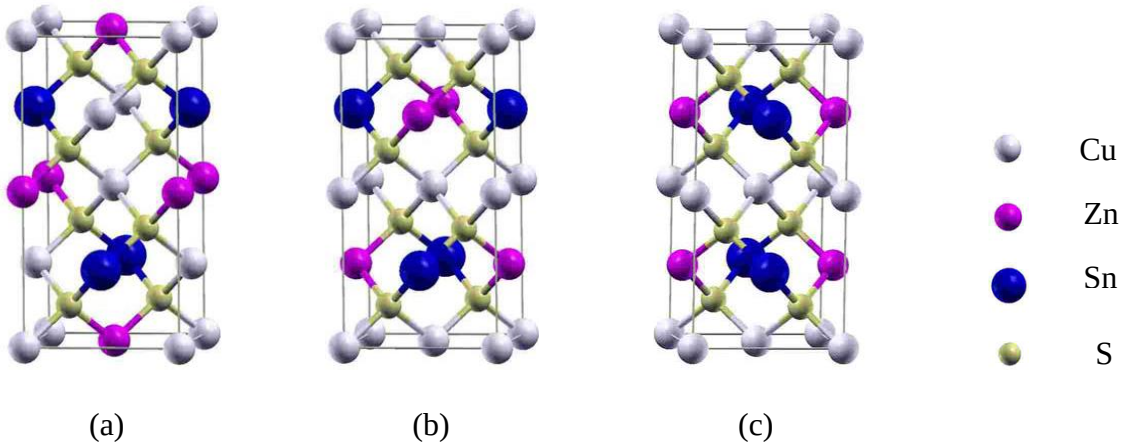


Figure 2.3 $I_2$-II-IV-$VI_4$ Crystal Structure: (a) Kesterite, (b) Stannite and (c) PMCA[44]

Kesterite and Stannite structures vary in the location of Cu and Zn atoms; while PMCA is varies from the Stannite structure by the location of Zn and Sn atoms.

The structural and electronic properties of the $I_2$-II-IV-$VI_4$ compounds, $Cu_2ZnSnS_4$ and $Cu_2ZnSnSe_4$, have been studied from first principle investigations. These studies have shown that there are three fundamental structures for quaternary $Cu_2ZnSnS_4$ and $Cu_2ZnSnSe_4$ compounds which obey the octet rule namely kesterite (KS), stannite (ST) and primitive mixed Cu-Au like structure (PMCA). Kesterite, having the lowest strain energy is the ground state structure. Although, a mixture of KS, ST and partially disordered kesterite (PD-KS) structures may exist in real samples due to similarities in energy [17,45]. This suggests that the lower band gap of the stannite structure compared to the kesterite may be one contributing factor to the low open circuit voltage (Voc) in these class of particles.

### 2.3.3. $Cu_2ZnSn(S_xSe_{1-x})_4$ Solar Cells

Solution processed CZTS,Se nanoparticles are derived from the more mature, and well-studied copper indium selenide ($CuInSe_2$) systems, through isoelectronic substitution of indium with the more earth abundant zinc and tin. In fact, solution processed CZTSSe nanoparticles follow synthesis procedures for CIGSe nanoparticles to produce structurally related material. Despite cost effective approach to produce materials for

solar cell applications, there still exists a sizable performance gap between CZTSSe and the more mature CIGSSe technologies.[6,22] A major efficiency limiting factor in inorganic thin-films is the presence of grain boundary defects in the absorber material. The high PCE of the extensively studied chalcopyrite, CIGSe devices have been attributed to its beneficial grain boundary properties.[46–48] The existence of neutral hole barriers in CIGSe devices due to Cu deficiency at boundary planes have been attributed to reduction in electron-hole recombination.[48] Moreover, extrinsic defects such as $Na^+$ at grain boundaries have also been shown to improve cell performance.[45] Due to similarities of crystalline structures of kesterite CZTSSe and chalcopyrite CIGSe, studies are underway to develop ways of engineering extrinsic grain boundaries in CZTSSe in order to passivate grain boundaries and improve performance.[38]

#### 2.3.3.1. Deposition Techniques

CZTSSe films have been deposited through PVD systems as well as solution deposition systems. Many PVD systems achieve a CZTS,Se thin absorber layer (CZTS,Se) by thermal deposition of precursors followed by annealing of material under inert gas, sulfur or selenium vapor.[7,49] These processes have several drawbacks including, complicated equipment and high cost, which makes them undesirable for scale-up. In order to address these issues, nanoparticles have been deposited through simple and low cost solution based approach including spray pyrolysis[50], spin coating[13,51] doctor blading[17] as well electrochemical deposition[52]. This solution based, non-vacuum depositions techniques, however, are limited by incorporation of impurities (carbon, oxygen, phosphorous) from solvents used, toxicity of chemicals.[53–55] Despite these drawbacks, solution processed CZTSSe nanoparticles are receiving increasing attention in recent years due to their low cost of production and scalability compared to more energy intensive vacuum deposition processes.

## 2.4. Colloidal Synthesis of Nanoparticles

Colloidal synthesis of nanoparticles initially consists of anion & cation precursors dissolved in organic solvents. The organic solvents serve as both surfactants and reducing agents during the synthesis of nanoparticles. Typically, cation and anion precursor solutions are heated at the desired temperature in an organic solvent, such as oleylamine (OLA), and injected into a hot solution (225°C-300°C) of typically the same solvent. Upon injection, nucleation occurs immediately, as the anion and cation precursors react to form monomers which supersaturate the solution. The particles are then allowed to grow at elevated temperatures, for a desired duration of time, typically from 0.5 to 1 hour. Immediately after precursor injection, the burst of nuclei relieves the supersaturation, and the subsequent drop in reaction temperature prevents more nuclei from forming resulting in reasonably monodispersed nanoparticles.[21,56] There are several mechanisms which have been proposed to describe the formation and growth of nuclei in solution based synthesis of nanoparticles. Ostwald ripening and digestive ripening are thermodynamically driven phenomenon which have been used to describe size and shape evolution of nanoparticles during wet synthesis.[57–59] Experimental and synthetic modelling have shown that in addition to thermodynamic effects, kinetics and reaction parameters such as, reaction time & temperature, as well as choice of capping ligands also determine size and structure of final nanoparticles.[60] In order to have better control of final nanoparticles in solution processed CZTSSe nanoparticles, it is crucial to understand the formation pathway as well as size and structure evolution of these nanoparticles.

### 2.4.2. Hot-Injection Method

Inorganic nanoparticles used in solar cells exhibit size, shape and compositional dependent optical and photochemical properties different from bulk material properties. For this reason various synthetic routes for nanoparticle manufacturing have been extensively investigated. It was in fact, the recognition of quantum confinement effects on optical properties of cadmium sulfide (CdS) nanoparticles which started the efforts to

synthesize semiconductor nanocrystals via wet chemistry routes.[56] Murray *et. al*. reported the hot-injection synthesis of cadmium chalcogenides (CdSe,S,Te) via injection of organometallic Cd and (S,Se,Te) precursors in a hot boiling organic solvent (TOPO).[61] This method of suspension of II-VI nanoparticles in organic solvents was then adopted to prepare other class of semiconductors: IV-VI ($SnS_2$), III-V (GaAs,InP), I-III-VI (CIGS,Se), I-II-IV-VI (CZTS,Se).[56]

Hot-injection synthesis technique has been widely used to produce monodispersed nanoparticles via a discrete nucleation step followed by growth of nanoparticles. This technique involves the injection of "cold" (room temperature) precursor solutions into a hot organic solvent (~300°C). Nuclei of the desired compound are formed immediately upon injection. The subsequent drop in temperature of the reaction solvent upon injection of precursors coupled with relief in supersaturation due to the initial nucleation burst, prevent the formation of new nuclei. Further growth of the nuclei takes place at reduced temperature. This method has been adapted for several class of semiconductors and has been reported to produce reasonably monodisperse final nanoparticles.[20,21,27]

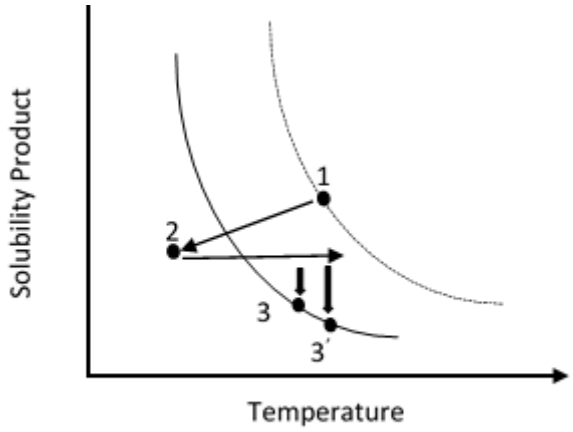


Figure 2.4 Solubility Product vs Temperature in Hot-Injection Synthesis.[56]

The points indicate: nucleation upon injection (1), subsequent cooling of solvent (1-2), growth of nuclei at two different temperatures (3&3')

### 2.4.3. Growth Mechanisms

As stated previously, Ostwald ripening is one mechanism, which has been used to describe size evolution of particles during a chemical or physical synthesis. This mechanism becomes increasingly more complex as the number of elements in the system increase. Colloidal synthesis of these multi-elemental systems, Ostwald ripening has been reported to be coupled with other competing mechanisms including, polymorphism, oriented attachment and crystal splitting.[62,63] Recently, there has been an interest in nanoalloys such as CZTSSe, CZTGeSe and SnSSe. These alloys offer the unique potential to alter optical properties by tuning the band gap of a semiconductor. In such complex systems, understanding the growth mechanism of nanoparticles during synthesis is crucial for producing nanoparticles with the desirable physical properties such as size, shape and composition, which directly affect the chemical properties of the resulting nanoparticles.[57]

In addition to size, shape and composition, another important characteristic of nanoparticles which needs to be controlled during wet synthesis is monodispersity. Monodispersed nanoparticles have been found to self-assemble into well-defined lattices. To this effect many synthesis processes employ digestive ripening techniques to produce monodispersed nanoparticles. This post synthesis process is used to modify polydisperse nanoparticles in a mechanism discussed previously, in order to narrow the size distribution of nanoparticles. In this process, the active ligand also known as ripening agent and the refluxing temperature have been shown to be important parameters that need to be manipulated to get the desired end result.[57] Monodispersed nanoparticles are especially crucial in solution processed particles through nanoparticle ink coating, where packing of particles during coating may influence densification patterns during subsequent annealing steps.

### 2.4.4. Challenges in Colloidal Synthesis of Nanoparticles

#### 2.4.4.1. Controlling Size & Structure

Control of structure and size dispersion of nanoparticles is essential when considering optimization and scale up of solution based processes. This involves rational design of experiments, varying of synthesis parameters coupled with first principle calculation and synthesis modeling to achieve a desired end result. Understanding the growth mechanism and morphology evolution of nanoparticles during a wet synthesis process is crucial to control size and structure of nanoparticles. The classical Ostwald ripening mechanism has been used to describe the formation of nanoparticles with nearly spherical morphologies.[57,58] In this thermodynamically driven phenomena, small crystals dissolve and redeposit onto larger particles over time. Small particles shrink while larger particles grow resulting in an increased average size of particles. The reverse, refluxing of polydisperse particles near the boiling point of the solvent used has been observed to produce monodispersed particles by the disintegration of larger particles via digestive ripening mechanism.[59] To this effect, reaction times area a key variable which have been manipulated to control particle size in solution processed nanoparticles.

In addition to thermodynamic effects, other factors such as kinetics and capping ligands play a key role in determining size and structure of nanoparticles. For example, the selective adsorption of capping ligands on certain faces in nanocrystals, reducing the surface energy of that particular face, has been attributed to the shape evolution of many inorganic crystals including CuS nanodisks[64] and gold nanoparticles[65]. Capping ligands also play a role in determining size of synthesized nanoparticles. It has been shown that the diameter of final nanoparticles can be raised by raising solute solubility i.e. increasing the concentration of free acid in hot-injection synthesis of various class of semiconductors including, II-VI[66], III-V[67] and IV-VI[68]. Capping ligands can also reduce growth by forming a barrier on atoms against reactants. For example, in hot-injection synthesis of CdSe nanoparticles, the capping ligand (TOPO) has been shown to reduce growth of particles by coordinating the surface of Cd atoms thereby forming a steric

barrier for reactants.[61] On the other hand, using solvents with short alkyl chains has been shown to lead to much faster growth of nanoparticles.[69]

#### 2.4.4.2. Controlling Crystal Phase

Different crystal phase in final particles could be a result of different reaction conditions. On one hand, it could be a result of the ligand passivation of certain facets of the crystal after nucleation while allowing others to dominate. As a result of two crystal phases occurring in a single structure, more complex 3D phases such as $Cu_2SnSe_3$ tetrapods, have been shown to form when a crystal nucleates in one phase and grows in a different phases.[70]

#### 2.4.4.3. Binary & Ternary Phase Formation in $Cu_2ZnSn(S_xSe_{1-x})_4$

A key parameter to consider when studying structural homogeneity of $Cu_2ZnSnS_4$ and $Cu_2ZnSnSe_4$ particles is the tetragonal distortion. In chalcopyrites, such as $CuIn_{1-x}Ga_xSe_2$ (CIGSe), deviation of lattice parameters, $c/2a$, from 1 is attributed to asymmetry in the top most valence band and formation of secondary phases.[8,44,71] In addition to disorders in the crystal structures themselves, formation of more favorable secondary and ternary phases also contribute to poor physical properties which translated to poor device performance. For example, formation of ZnS(Se) phase in CZTSSe particles, a high band gap and low conductivity material, is attributed to high series resistance and formation of Cu-Sn-S(Se) phase, a low band gap and high conductivity material, is attributed to lowering open circuit voltage (Voc).[71] Phase inhomogeneity in the absorber material is one of the key limiting factors in achieving high efficiency solar cells. Formation of various phases, as previously stated, leads to poor device properties by creating multiple band gaps in the absorber material. These defects act like recombination sites and inhibit the maximum amount of current which can be collected from the solar device.

# CHAPTER 3. MOTIVATION & METHODOLOGY

## 3.1 Motivation & Approach

A suitable colloidal nanocrystal ink for use in a scalable coating process is a key step in the development of low-cost solar cells. Although solution based synthesis of CZTS has shown great promise, efficiencies for this system are still significantly lower than the more advanced CIGSe system.[6,22] Devices from CZTS nanoparticles are finished by undergoing a high temperature annealing step under selenium vapor in order to induce grain growth. During this process, sulfur is replaced with selenium producing CZTSSe film. This crucial annealing step produces large grains of about 100-200 μm in diameter and reduce the number of grain boundaries which generated carriers would have to overcome in order to be collected at the contacts. There is little control over elemental composition of the material during this annealing step. One approach to address this may be to start with CZTSSe nanocrystals because then the composition uniformity is ensured even at the atomic levels.

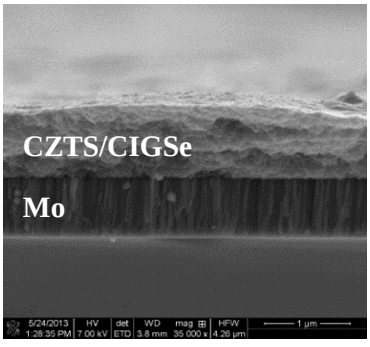


**(a) Cross-Section of Coated Film**

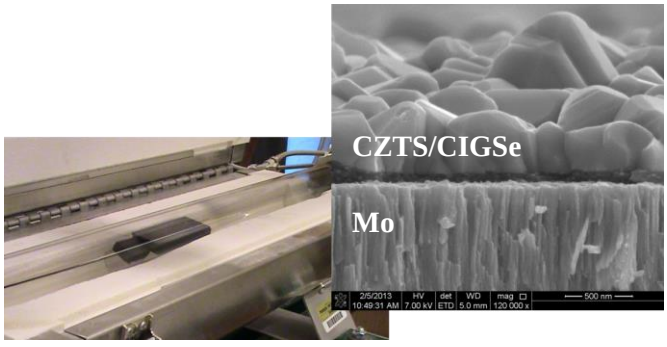


**(b) Cross-Section of a Film Post Selenization**

Figure 3.1 Illustration of Grain Growth during Selenization

Another aspect of solution based synthesis of CZTSSe nanoparticles that is of challenge is the complexity of a quinary system. In this system, it is difficult to control growth of the main desired phase in competition with binary, ternary and quaternary phases. Enhancing the purity of the nanoparticles and producing CZTSSe nanoparticles with randomly distributed sulfur and selenium atoms may lead to better device performance by reducing defect in the lattice that may arise due to lattice mismatch or phase segregation. These defect sites could potentially limit efficiency of the final device by serving as recombination sites and lowering carrier density.

## 3.2 Experimental Details

Experiments were designed to 1) test the role of anion precursor solution in the formation of uniform phase CZTSSe nanoparticles, and 2) to understand growth mechanism of kesterite phase CZTSSe nanoparticles. CZTSSe nanoparticles were synthesized with the use of anion precursors prepared through various routes.

### 3.2.1. Materials

Copper II acetylacetonate (99.99%), tin (IV) bis(acetylacetonate) dichloride (98%), zinc acetylacetonate hydrate (99.995%), sulfur (99.99%) selenium (99.99%) ethanethiol (98%) were purchased from Sigma Aldrich. Oleylamine (80-90%) was purchased from Alcros. All precursors were used as shipped without any further purification, with the exception of oleylamine which is treated to freeze-pump-thaw cycle to remove light impurities.

### 3.2.2. Nanocrystal Synthesis

*Cation Precursor Preparation*

1.32 mmols copper, 0.75 mmols tin and 0.78 mmols zinc were dissolved in 6 mL oleylamine in a separate one neck flask and heated to 60° C under constant stirring to insure complete and uniform dissolution.

*Anion Precursor Preparation*

Anion solutions were prepared in one of three different ways discussed below.

Method 1

The desired amount of elemental sulfur or selenium were weighed in a glove box and placed in a round bottom flask. OLA was added to produce a sulfur or selenium concentration of 1 M and the flask is sealed with a rubber septa. Outside the glove box, the mixture is heated to 60 °C under constant stirring. Sulfur is soluble in OLA at this temperature and forms a dark, red, transparent solution. Selenium remains insoluble and exists as a dispersion.

Method 2

The desired anion precursor was weighed and placed in a round bottom flask inside a glove box. OLA was added to produce a final sulfur or selenium concentration of 1 M and the flask is sealed with a rubber septa. Outside the glove box, a syringe was evacuated and purged with inert gas, and the desired amount of thiol was injected into the sealed round bottom flask. The solution was then heated at 60 °C under an inert gas blanket, i.e. while maintaining constant purging with inert gas.


Figure 3.2 Apparatus for Anion Solution Preparation using Method 2

Method 3

The desired concentrations of sulfur and/or selenium were weighed inside a glovebox and added into a three neck flask and mixed with oleylamine to yield a 1M total concentration of sulfur, selenium or sulfur+selenium (S+Se) solution. The flask was attached to a condenser and sealed. Outside the glove box, the reaction flask was purged with inert gas at room temperature through the use of a Schlenk line. A syringe was evacuated and purged with inert gas; excess amount of ethanethiol (~25% excess relative to anions) was injected into the mixture to induce reduction of the chalcogen(s) and formation of the alkylammonium-anion complex.[72,73] The mixture was heated to the desired temperature (60 °C for sulfur solution or (S+Se) solution, and 120 °C for just selenium solution) and purged of reactive disulfide and thiol compounds.

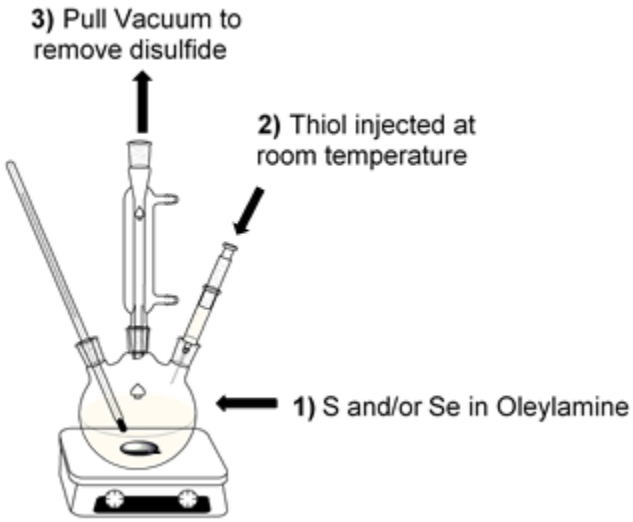


Figure 3.3 Anion Precursor Preparation using Method 3

Reduction of anions takes place at room temperature. Removal of consequent disulfide formed may be removed by elevating the temperature and/or lowering the pressure of the system.

*Nanoparticle Synthesis*

12 mL OLA was added to a 3-neck flask under inert environment followed by vacuum pumping and $N_2$ bubbling at room temperature. A secondary vacuum /purge cycle was done at reflux temperature, 120°C. The temperature was raised to reaction temperature and the desired amount of anion mixture was injected rapidly, followed by the cation mixture injection. Typically, excess amount of anions relative cations (about 50% excess) are injected. A significant drop in temperature observed upon injection, quenches the reaction and minimizes subsequent nucleation resulting in monodispersed nanoparticles. The reaction is typically ran for 1 hour at 250°C and cooled to room temperature. After cooling to room temperature, nanoparticles were washed with hexane/IPA and centrifuged for 5 minutes at 1400 rpm in order to remove solvent and unreacted precursors. If the supernatant from the initial collection step appears dark, it is transferred to a different centrifuge tube and washed separately to collect the small particles. The final particles collected were dried under a nitrogen blanket and stored in a vacuum desiccator for characterization.

### 3.2.3. Characterization

The crystallographic information of the nanoparticles was obtained from powder X-ray diffraction (PXRD) operated at 40 kV and 44 mA. Elemental composition of the nanoparticles was obtained by energy-dispersive X-ray spectroscopy (EDS).And finally, the vibrational pattern of the particles was obtained via Raman spectroscopy using a HORIBA Jobin Yvon LabRam HR800 system with an excitation wavelength of 632.81 nm.

# CHAPTER 4. RESULTS & DISCUSSION

## 4.1 Synthesis of High Purity $Cu_2ZnSn(S_xSe_{1-x})_4$ Nanoparticles

Wet synthesis of multi-element nanoparticles suffer from several drawbacks one of which is the formation of undesirable phases during synthesis. This is made even more complicated in a quaternary, mixed chalcogen system such as kesterite CZTSSe. Herein, we report the preparation and characterization of high purity CZTSSe nanoparticles through the use of a uniform mixed chalcogen precursor solution. This conclusion was based on the singularity of the diffraction peaks for this sample in XRD (Figure 4.3), as well as lack of distinct secondary or ternary shifts in Raman (Figure 4.4). The role of anion precursor solution in the structure of final nanoparticles is also investigated and discussed in the proceeding section.

In order to produce a uniform sulfoselenide precursor solution, sulfur and selenium were prepared together in a mixture of amine and light thiol using Method 3. This method is adapted from a selenium dissolution method reported previously.[72,73]

*Selenium Dissolution Method*

With increasing interest in selenide based nanoparticles in various industries including photovoltaics and biomedical research, there has been a need for well dissolved selenium solution. Traditionally, selenium precursors have been prepared using hazardous and unstable chemicals such as alkylphosphines (TOP) or through the use of organic solvents such as OLA.[41,61] It has been reported that selenium can be successfully reduced by ultrasonication of selenium powder in a mixture of $NabH_4$ and OLA.[28] These methods suffer from several drawbacks including cost, toxicity, and phosphorous contamination of

the final particles. In addition, selenium precursor solution prepared by alkylthiol reduction of selenium powder has been shown to be highly reactive in hot-injection synthesis of selenide semiconductors.[73]

Walker *et. al*, has reported a similar process, where by selenium was reduced in an amine+thiol mixture followed by the removal of unreacted thiol and disulfide to yield a sulfur free selenium solution.[73] Analysis of the selenium solution in gas chromatography Mass Spectrometry (GC-MS) soon after dissolution in amine + thiol mixture indicates the formation of disulfide compound. After a vacuum/purge cycle at elevated temperatures, GC-MS data indicates the disappearance of both the thiol and disulfide peaks. Based on this observation as well as additional supporting data from (Fourier Transform Infrared) FTIR, the following reduction mechanism for selenium has been proposed for selenium.

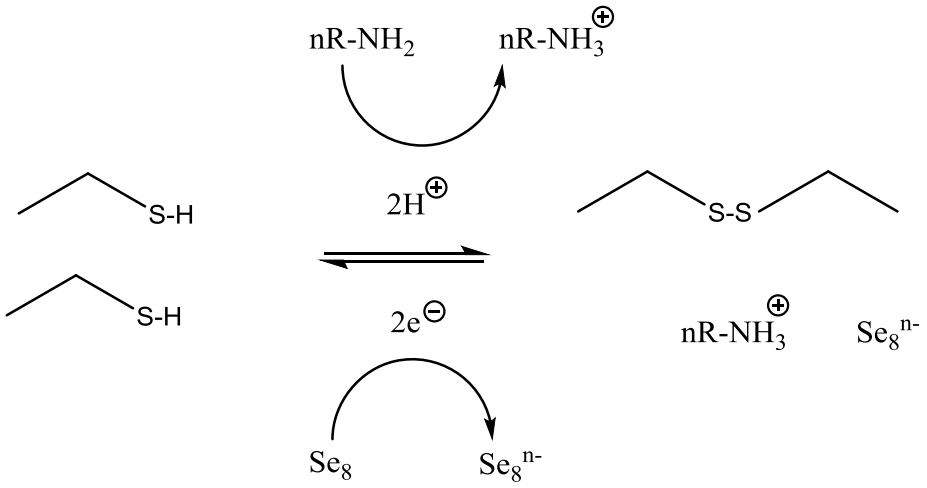


Figure 4.1 Proposed Mechanism of Selenium Reduction [73]

In this study, the reduction process reported by Walker *et. al*., was adopted to prepare a uniform sulfoselenide precursor solution. Preliminary analysis of sulfur solution prepared in an amine + thiol mixture through Electrospray Ionization Mass Spectrometry (ESI-MS) as well as Atmospheric Pressure Chemical Ionization (APCI ) suggest a sulfur reduction mechanism similar to what was proposed by Walker *et. al*. (Figure 4.2) Further investigation is underway to better understand this particular system and to find evidence to either support or refute this hypothesis.

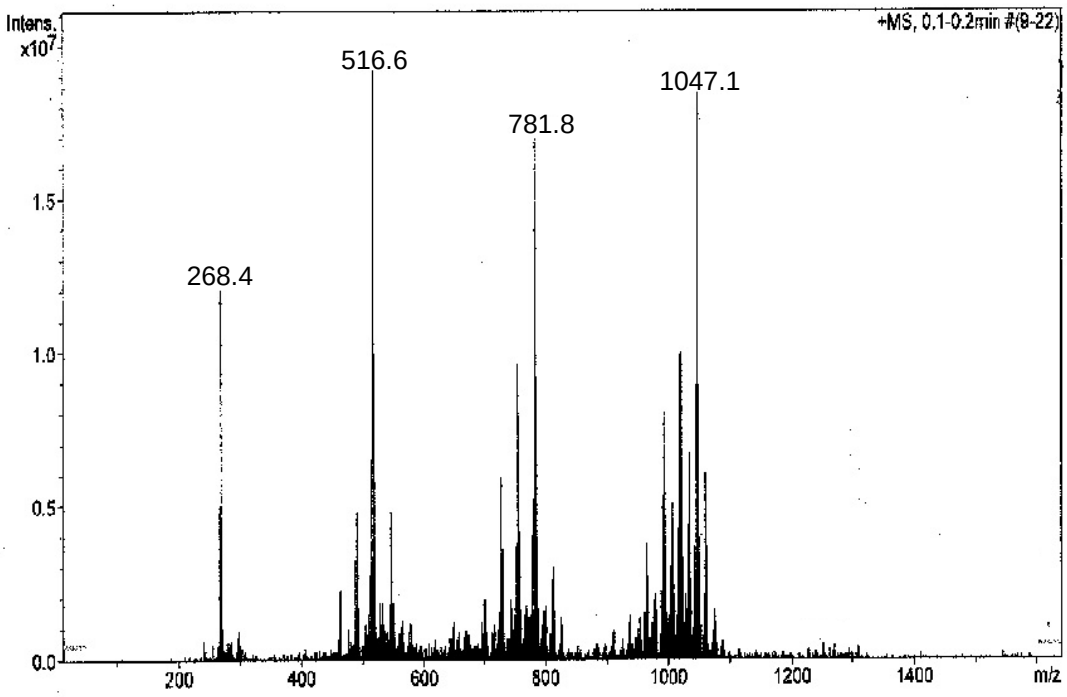


Figure 4.2 ESI-MS Spectra of Sulfur Dissolved in a Mixture of Amine + Thiol.

Through the use of elemental composition calculation tools, analysis software such as ChemBioDraw as well as through manual deconvolution, the peaks listed in Table 4.1 have been assigned to corresponding compounds listed in Table 4.1. It is important to note that, for higher mass to charge (m/z) the mass-spectroscopy (MS) data reported must be coupled with other analysis tools such as nuclear magnetic resonance (NMR) to get conclusive information.

Table 4.1 Proposed Structures for m/z Observed from ESI-MS Analysis of Sulfur Solution.

| m/z | Proposed Structure |
|---|---|
| 268.4 | $RNH_3^+$, $C_{18}H_{38}N$, R=$C_{18}$ chain |
| 516.6 | *RNHR*, $C_{36}H_{70}N$, R=$C_{18}$ chain |
| 1047.1 | $nRNH_3^+ \xrightarrow{S_8} (RNH_3^+)(RNH-S_8^-)(R'NH_3^+)$, R=$C_{18}$ chain; R'=$C_{17}$ chain |

The first peak of 268.4 m/z can be attributed to a protonated OLA group. The second peak may be a result of two amine groups coming together and giving off ammonia ($NH_3$), which is commonly observed during ESI-MS analysis of amines. An additional loss of $H_2$ group can result in a m/z of 516.6. The peak at 1047.1 may be a result of an amine group complexed with an alkylammonium sulfide group as shown in Table 4.1. Based on this preliminary study of the anion solution via mass spectrometry as well as sulfur reduction mechanisms reported in literature[74], we assume that the sulfoselenide precursor solution exists as an alkylammonium chalcogen complex.

*Synthesis Approach for High Purity CZTSSe Nanoparticles*

In order to produce a uniform sulfoselenide precursor solution, sulfur and selenium were prepared together in a mixture of amine and light thiol using Method 3. CZTSSe nanoparticles synthesized using this uniform mixed chalcogen solution were found to have a narrow phase distribution, as observed from XRD (Figure 4.3) and Raman spectroscopy (Figure 4.4).

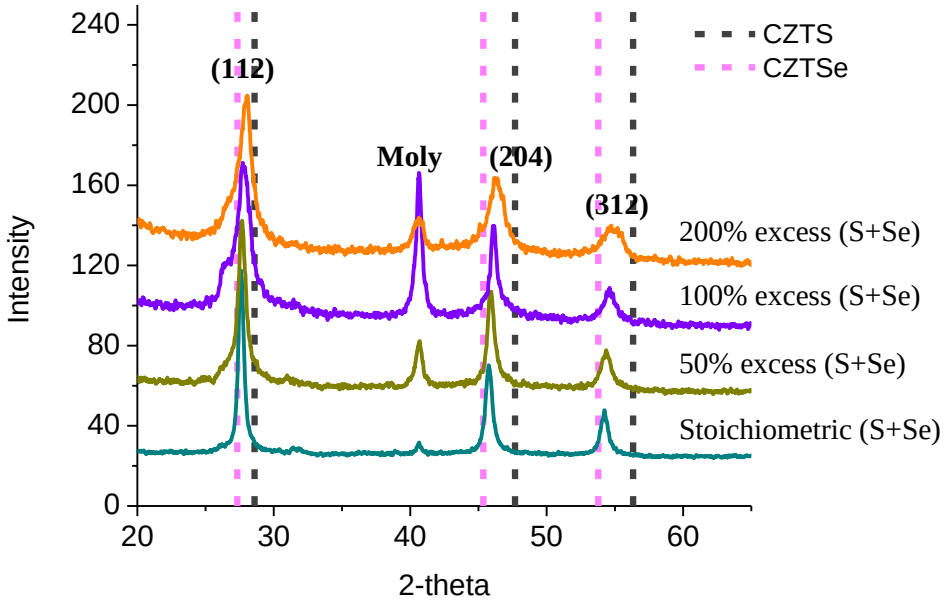


Figure 4.3 XRD spectra of CZTSSe nanoparticles with varying excess anion (S+Se).Reaction temperature, 250 °C. Reaction time, 1 hour.

The replacement of the smaller sulfur atoms (1.84 Å ionic radius size) by the larger selenium atoms (1.98 Å ionic radius size) causes the expansion of lattice parameters causing a shift in diffraction angle to a lower 2θ value with increasing selenium content.[27] It can be observed from XRD that the position of the CZTSSe peaks systematically shifts to a higher diffraction angle with increasing amount of anion injection, i.e. increasing sulfur incorporation, as reported in literature.[27,28,75] The shoulder observed on the (112) plane may be a result of lattice dislocations related to cation disordering with similar stacking faults observed in CIGSe and $CuInSe_2$ systems.[26] The diffraction peak location between that of standard CZTS and CZTSe peak locations (ICSD database) was observed for all major peaks (112), (204) and (312), for CZTSSe nanoparticles with 200% excess anion added. XRD data for CZTSSe nanoparticles with S:Se ratio of 1:3 and 3:1 can be found in Appendix A.1 and A.2 , respectively. The diffraction pattern in this samples did not display any peak splitting; however, a slight non-symmetry of the some peaks in

these samples suggests the presence of small amounts of undesirable phases, which were not detected in Raman.

The elemental composition of the nanoparticles obtained by energy dispersive X-ray spectroscopy (EDS) (Table 4.3) revealed that addition of excess anion to the reaction was needed to balance the incorporation of sulfur and selenium into the system. Assuming actual S:Se ratio in final film is same as the amount added during reaction, estimated locations of major CZTSSe peaks were calculated using Vegard's law and Bragg's law (Table 4.2). The estimated 2-theta values for the synthesized CZTSSe nanoparticles match very closely with the peak locations observed from PXRD analysis CZTSSe nanoparticles with 200% excess anion added.

$$Vegard's\ law: \quad d_{CZTSSe} = x * d_{CZTS} + (1-x)d_{CZTSe} \qquad \text{(eq.1)}$$

$$Bragg's\ law: \quad n\lambda = 2dsin\theta \qquad \text{(eq. 2)}$$

Here "d" stands for lattice spacing of individual components (CZTS and CZTSe) while "x" is the relative ratio of the components, θ is diffraction angle and nλ, path length difference, is equal to 1.54056 Å.

Table 4.2 Estimated and actual diffraction angle locations of major peaks for $Cu_2ZnSn(S_xSe_{1-x})_4$; x=0.5 with 200% excess anion solution added. Estimated peak locations were calculated using Vegard's Law and Bragg's Law. Actual peak location were obtained by fitting a Gaussian curve to the data through OriginPro software.

| *Peaks* | *d-value( Å)* | *sinθ* | *Estimated Peak Location (2θ)* | *[2]Actual Peak Location (2θ)* |
|---|---|---|---|---|
| *112* | 3.190 | 0.241 | 27.944 | 27.917 |
| *204* | 1.953 | 0.394 | 46.469 | 46.324 |
| *312* | 1.664 | 0.463 | 55.170 | 54.782 |

Further investigation was done using Scanning Electron Microscopy-Electron Dispersive X-ray Spectroscopy (SEM-EDS) analysis to determine the elemental composition of the synthesized particles. Table 4.3 summarizes the atomic ratios determined from EDS analysis for all the synthesized samples normalized to tin.

Table 4.3 EDS data for CZTSSe Nanoparticles with Varying Excess Anion (S+Se) Added

| | *CZTSSe (S:Se of 1:1)* | | | | |
|---|---|---|---|---|---|
| | ***Cu*** | ***Zn*** | ***Sn*** | ***S*** | ***Se*** |
| *Theoretical* | 1.76 | 1.05 | 1 | 4 | |
| *Stoichiometric (S+Se)* | 1.91 | 0.56 | 1 | 1.04 | 1.95 |
| *50% excess (S+Se)* | 2.11 | 1.09 | 1 | 1.19 | 2.08 |
| *100% excess (S+Se)* | 1.86 | 1.19 | 1 | 1.57 | 2.32 |
| *200% excess (S+Se)Large Particles* | 1.79 | 1.21 | 1 | 1.81 | 2.56 |
| *200% excess (S+Se)Small Particles* | 1.47 | 0.92 | 1 | 1.59 | 2.16 |

It can be observed from EDS that even with excess amount of sulfur added, the amount of selenium is still slightly more than that of sulfur. This could be due to loss of sulfur as $H_2S$ or the presence of unreacted selenium. The overall elemental composition of the film was greatly varied as a result of varying amounts of anion solution added. The low sulfur incorporation relative to selenium even for 200% excess anion injected may be attributed to high volatility of sulfur, loss of sulfur in the form of $H_2S$ in these systems or due to the

[2] Preliminary results from initial synthesis

presence of unreacted selenium.[74] An extra washing step, using a light thiol + amine mixture may be necessary to remove undreacted selenium prior to EDS analysis of these nanoparticles.

To further investigate phase purity of synthesized particles, the vibrational properties of the synthesized particles was studied using Raman spectroscopy. Analysis of purity of samples using this tool suggest that CZTSSe nanoparticles synthesized with S:Se ratio of 1:1 (Figure 4.4) do not appear to have binary or ternary phases especially for higher amounts of excess anion solution added. If present these phases may be in very small amounts. The A1 symmetry modes in the CZTSSe nanoparticles show a gradual shift to higher frequency side with increasing sulfur content, as previously reported.[27] This trend is more obvious when comparing in CZTSSe prepared with S:Se ratios of 1:3(Appendix B.1) and 3:1 (Appendix B.2). It is important to note here that these S:Se ratios refer to amounts of sulfur and selenium used in the reaction and not the final composition of the particles. In fact, in the reaction, sulfur incorporation has been found to be poor. Therefore, excess anions relative to cations are usually injected into the reaction system to balance the incorporation of sulfur and selenium in the system.

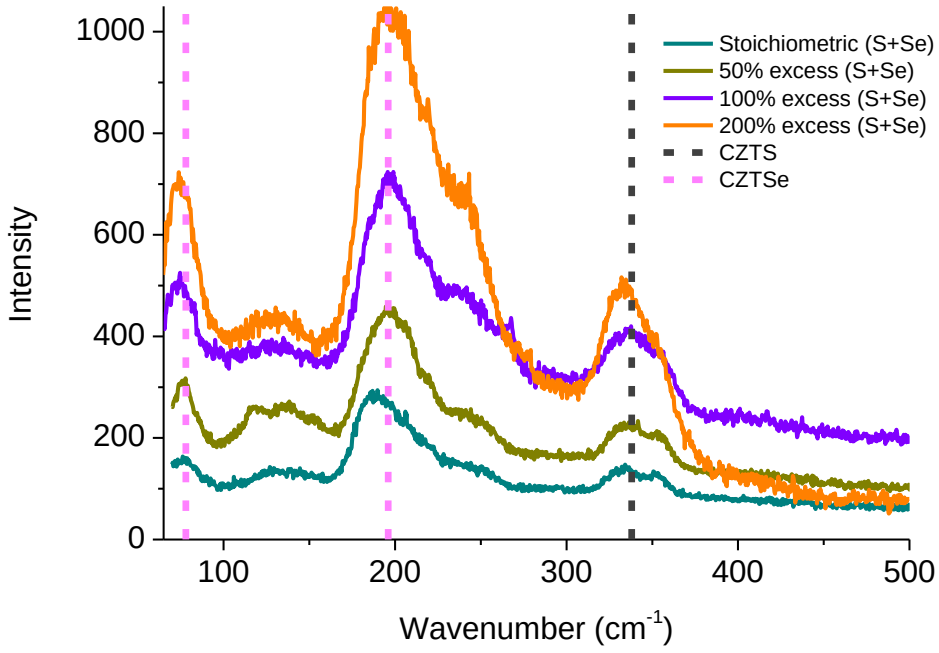


Figure 4.4 Raman shift of CZTSSe nanoparticles with varying excess anion (S+Se). Reaction temperature, 250 °C. Reaction time, 1 hour.

The Raman spectrum (Figure 4.4) shows a strong peak at 338 $cm^{-1}$ and 196 $cm^{-1}$, which corresponds to the A1 mode of CZTS and CZTSe respectively. The A1 symmetry modes in the CZTSSe nanoparticles show a gradual shift to higher frequency side with increasing sulfur content, as previously reported.[24] This trend is more obvious when comparing in CZTSSe prepared with S:Se ratios of 1:3 and 3:1 (Appendix B.1 and B.2).

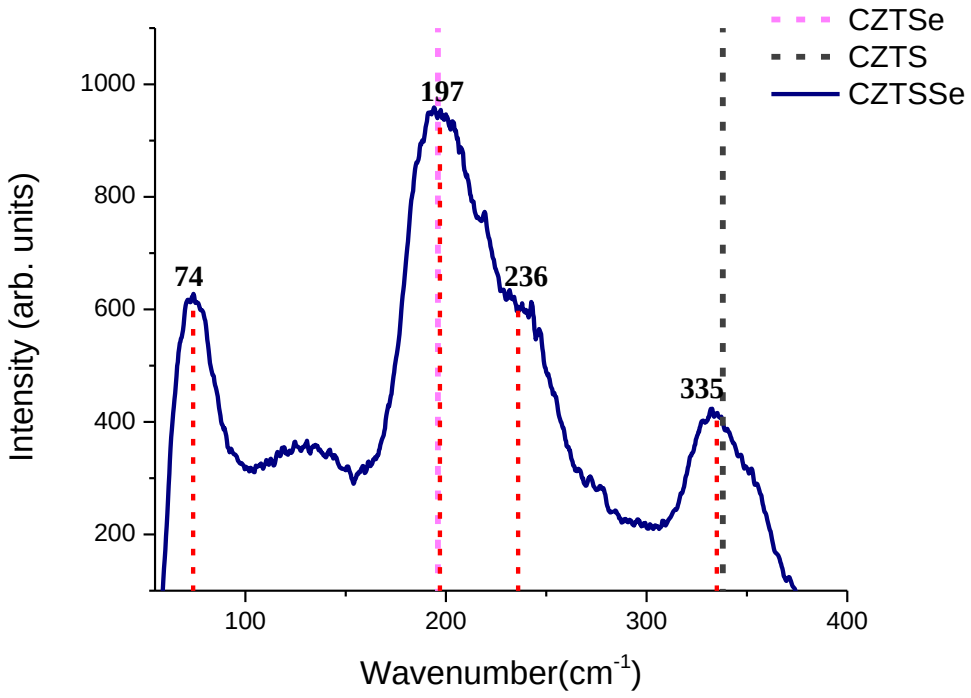


Figure 4.5 A Closer Look at Raman shift of CZTSSe nanoparticles with 200% excess (S+Se) injected.

Dotted lines represent standard shifts for A1 symmetry modes of CZTS and CZTSe. Dashed lines represent peaks identified using peak fitting tool in OriginPro (numerical values shown).

A closer look of CZTSSe nanoparticles with 200% excess (S+Se) injected (Figure 4.5) using OriginPro peak analysis tool revealed additional peaks. The peak at 74 $cm^{-1}$ closely matches the CZTSe peak at 78 $cm^{-1}$. The low intensity broad peak from ~124-140 $cm^{-1}$ may be a result of amorphous Se which typically has a Raman shift of 138 $cm^{-1}$. A peak at 236 $cm^{-1}$ is present and may correspond to $Cu_2SnSe_3$ (236 $cm^{-1}$) but could also be a result of trigonal Se which has peaks at 233 $cm^{-1}$ and 237 $cm^{-1}$. Findings from this analysis suggests lack of any binary phases and perhaps the presence of a $Cu_2SnSe_3$ (CTS) phase.

## 4.2 Investigating the Role of Anion Precursor Nanoparticle Synthesis

In order to determine the role of anion precursors in our system, sulfoselenide precursor solution was prepared via different routes and/or introduced into the reaction system in different ways. The crystallographic information of the synthesized nanoparticles was obtained from powder X-ray diffraction (PXRD) operated at 40 kV and 44 mA. Figures 4.6-4.8 show, X-ray diffraction patterns for CZTSSe nanoparticles synthesized through four different approaches.

Case 0: S in OLA and Se in OLA prepared separately using Method 1 and injected simultaneously into reaction flask.

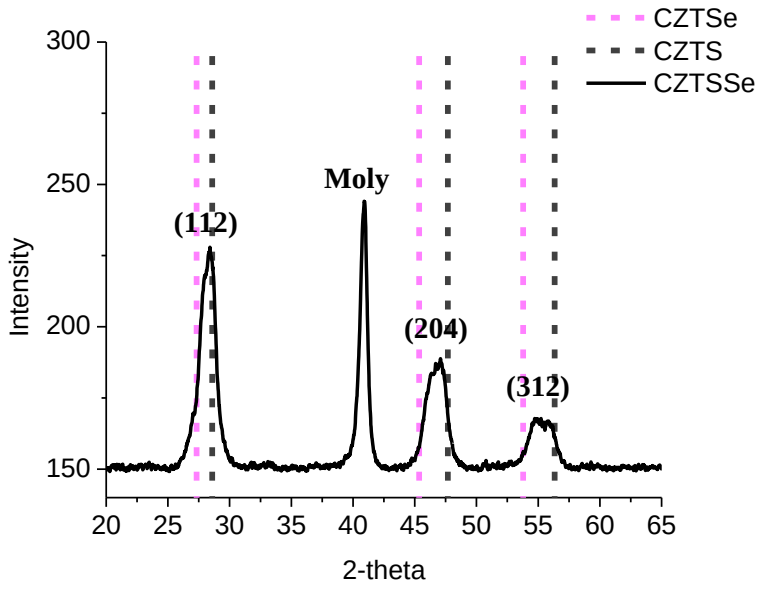


Figure 4.6 XRD spectra of CZTSSe nanoparticles with 50% excess anion (S+Se).Reaction temperature, 225 °C. Reaction time, 1 hour. (Trendline: 5 point moving average)

The diffraction pattern for CZTSSe nanaoparticles prepared using this route shows some irregularities and peak splitting, indicative of phase segregation in the crystal lattice. In this approach, sulfur was prepared in OLA at 60 °C, which is standard for most hot-injection reactions involving sulfur. Selenium, however, is insoluble in OLA at 60 °C and only partially soluble at elevated temperatures. This has resulted in less selenium

incorporation in the crystal lattice causing the diffraction peak to shift to the right, near the position of the CZTS phase. In order to address this, a selenium dissolution approach described previously involving the use of amine and thiol mixture was adopted to produce a well dissolved selenium solution and improve selenium incorporation in the final nanoparticles (Figure4.3).

Case 1: S in OLA using Method 1 and Se in OLA+thiol using Method 3 prepared separately, mixed together before injection into reaction flask.

In this approach, a standard sulfur solution was prepared in OLA at 60 °C (Method 1). In a separate flask, selenium was dissolved in a mixture of OLA and ethanethiol as described in Chapter 3 (Method 3). The mixture undergoes several vacuum/purge cycles during heating in order to remove unreacted thiol and disulfide and cooled to 60 °C. The two anion solutions are then mixed together to form a homogenous chalcogenide mixture and injected into the reaction vessel at the desired temperature.

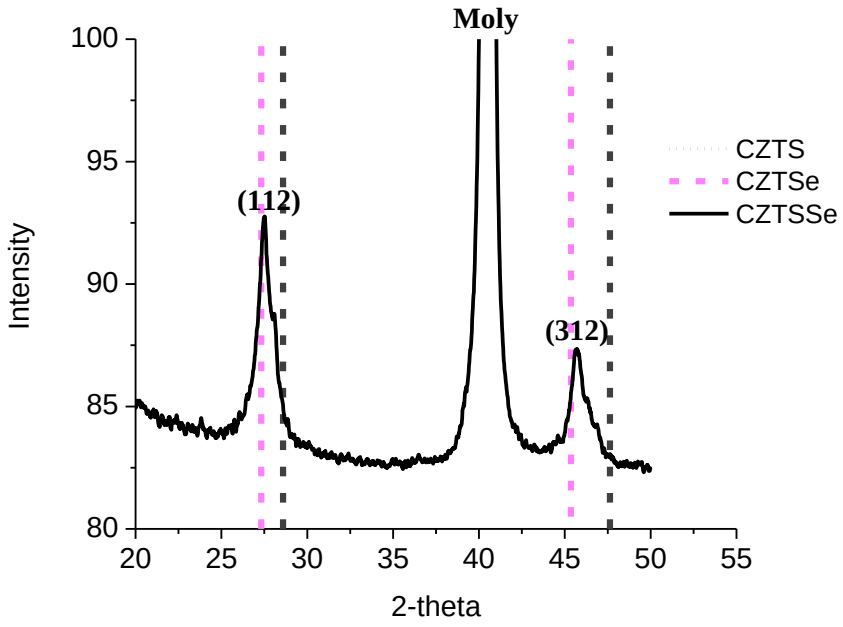


Figure 4.7 XRD spectra of CZTSSe nanoparticles with 33% excess anion (S+Se).Reaction temperature, 250 °C. Reaction time, 0.5 hour.

For the described reaction conditions, Figure 4.7 shows the diffraction pattern for the resulting nanoparticles. The diffraction pattern for CZTSSe nanoparticles in Case 1, shows that the peaks are located at a lower diffraction angle, closer to the CZTSe line indicating more selenium incorporation. The shoulder on the right side of the main (112) peak suggests the presence of a less pronounced, higher sulfur content CZTSSe phase in the particles. Asymmetry of the (204) peak can also be an indication of a wide phase distribution and presence of other phases.

One challenge during synthesis of sulfoselenide nanoparticles has been balancing the incorporation of the chalcogen in order to produce particles with randomly distributed sulfur and selenium atoms. Rhia et. al., has reported that compositionally controlled CZTSSe nanoparticles were obtained only when sulfur and selenium were sonicated together in order to balance the relative reactivity of the two elements. From our own observation, even in with the use of a uniform sulfoselenide precursor solution, the system favors selenide formation. In fact, excess amounts of anion precursor must be introduced into the reaction system in order to improve sulfur incorporation. This may be partly due to loss of elemental sulfur or loss of sulfur in the form of $H_2S$ as observed in wet synthesis of CZTS nanoparticles.[74]

Case 3: S in OLA+thiol and Se in OLA+thiol prepared separately using Method 2, injected simultaneously into reaction flask.

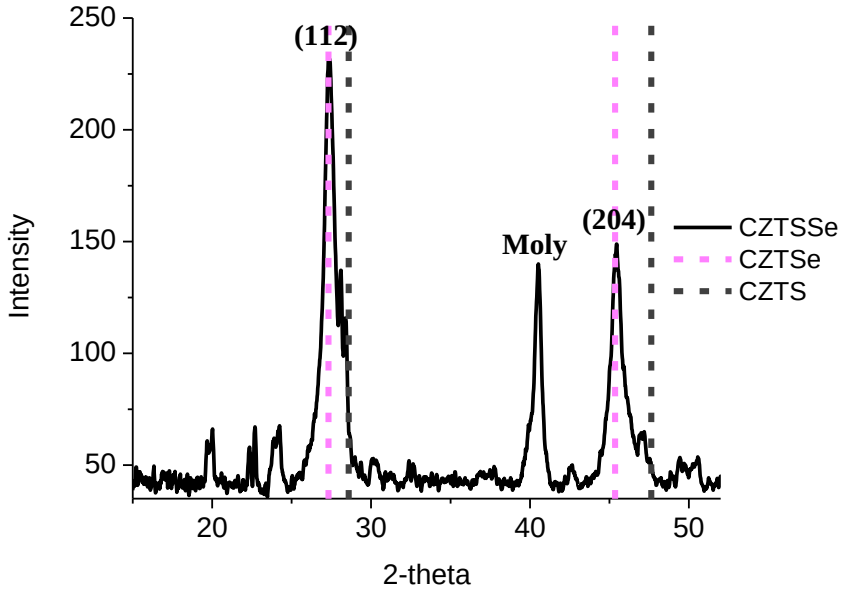


Figure 4.8 XRD spectra of CZTSSe nanoparticles with 50% excess anion (S+Se).Reaction temperature, 250 °C. Reaction time, 1 hour.

In case 3, both sulfur and selenium were prepared in a mixture of amine + thiol as in Method 2 described in Chapter 3. The precursors were injected simultaneously, but separately at reaction temperature. The diffraction pattern from the CZTSSe nanoparticles synthesized using this approach not only show poor sulfur incorporation but also the presence of additional undesirable phases, possibly due to thiol & disulfide contamination.

The results from the above experiments indicate the need for a uniform, mixed chalcogen mixture prior to reaction in order to yield high purity CZTSSe nanoparticles with narrow phase distribution.

## 4.3 Sulfur & Selenium Reactivity Study

Another important factor that is of interest in wet synthesis of CZTSSe nanoparticles is the relative reactivity of sulfur and selenium. It has been observed in this study and also reported in literature that selenium is more readily incorporated in these systems.[28] This phenomenon was investigated further through the synthesis of CZTS nanoparticles with subsequent introduction of different concentrations of selenium into the system and observing the structural evolution of the particles through time. The partnered experiment, whereby sulfur is introduced after the initial formation of CZTSe particles adds further valuable information into understanding the problem.

For different amounts of selenium added into already prepared CZTS nanoparticle solution, it was observed that a shoulder is formed to the left of all major kesterite peaks in PXRD indicating the formation of a separate CZTSe phase. This shoulder is more pronounced with the utilization of increasingly excess amount of selenium added to the CZTS particles, and continues to grow during the reaction period (Figure 4.9). The reverse reaction, where different amounts of sulfur was injected into an already prepared CZTSe solution, did not cause a shift in the diffraction pattern of the particles or an observed secondary phase formation(Figure 4.10).

CZTS nanoparticles were synthesized using standard wet synthesis route described in Chapter 3, section 3.2.2. After a 1 hour reaction period, different amounts of selenium were injected into the reaction mixture. Aliquots were collected at different stages of the reaction, and the crystal structure of those aliquots were analyzed in XRD. The sample with the highest concentration of selenium added (S:Se=1:2), yielded a diffraction pattern showing two distinct phases in XRD. At 5 minutes elapsed time, a small shoulder appears on the left side of the main CZTS peaks. With increasing reaction time, this shoulder grows and forms a distinct CZTSe phase (Figure 4.9).

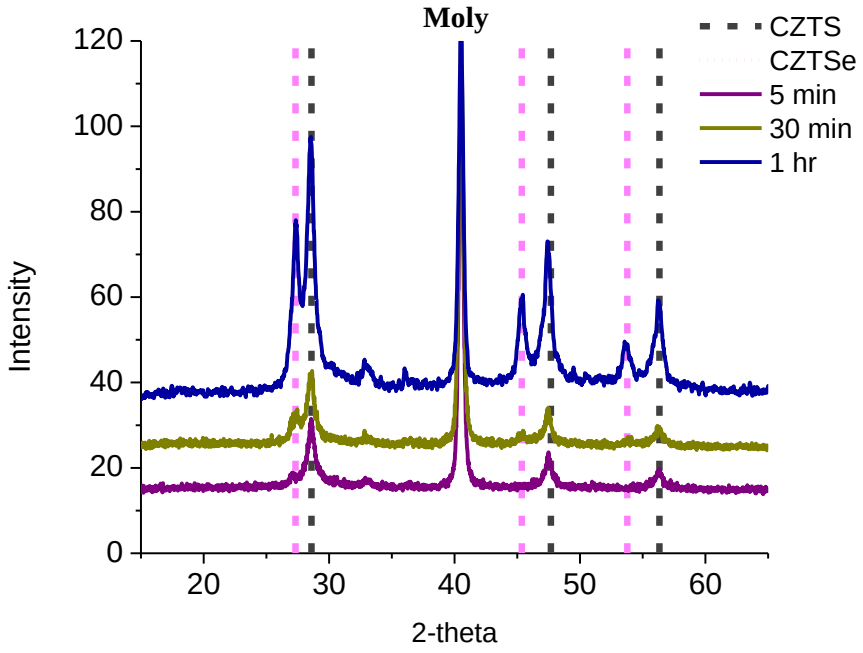


Figure 4.9 XRD spectra of CZTS nanoparticles at various elapsed time after excess selenium injection. (Trendline: 5 point moving average).

Furthermore, CZTS particles were prepared using standard recipe reported in literature and described in Chapter 3.After 1 hour reaction at 250 °C , an aliquot was taken(t=0) followed by excess selenium injection (S:Se=1:1.33) (Appendix A.3). After selenium injection, aliquots were taken at 5 min, 12 min, 25 min, 1 hr and the reaction was allowed to continue for 5 more additional hours. In this experiment, a CZTSe phase appears as a small shoulder and continues to grow. After 6 hours of reaction time, the selenide phase becomes dominant, while a less dominant sulfide phase exists.

In cases where a lower concentration of selenium was injected (S:Se=1:1), a small distinct peak appears on the left side of the (112) peak. As the reaction is allowed to progress, the peak appears to merge with the CZTS peak forming a shoulder. Analysis of the diffraction angle location for this small peak, suggests the formation of a $Cu_xSe$ phase, which then either grows into a CZTSe phase or remains as a binary impurity in the final nanoparticle (Appendix A.5). This hypothesis is plausible because formation of CuSe phase has been observed in situ energy-dispersive X-ray diffraction of a CZTS film during an annealing process under selenium rich vapor.[76] There lies a need to further investigate the compositional makeup of the particles.

In the reverse reaction, where varying amounts of sulfur was introduced to CZTSe nanoparticles, the diffraction pattern in XRD indicate no change in the structure or composition of the particles; the CZTSe phase remains intact.

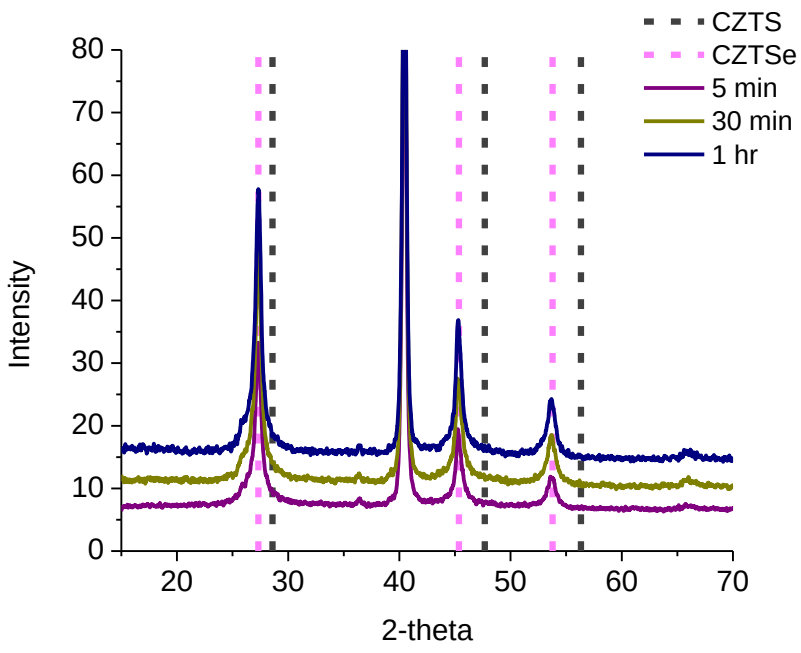


Figure 4.10 XRD spectra of CZTSe nanoparticles at different stages of structural evolution after excess sulfur injection. (Trendline: 5 point moving average.)

During the above reaction, deposition of a yellow substance on the reaction apparatus was observed, potentially suggesting loss of elemental sulfur. To test if loss of sulfur was in fact the reason for lack of sulfur incorporation, CZTSe nanoparticles were prepared and injected into a sulfur rich solution. For this reaction aliquots were taken at 5 min, 12 min, 25 min, 1 hr and 5 hrs. Analysis of the structure of resulting nanoparticles indicate that the CZTSe phase remained intact throughout the reaction (Appendix A.4), suggesting that kesterite CZTSe, once formed, is highly favorable and stable phase in these systems.

# CHAPTER 5. CONCLUSIONS

## 5.1 Summary & Conclusions

In summary, high purity mixed chalcogen, solution processed $Cu_2ZnSn(S_xSe_{1-x})_4$ nanoparticles, have been successfully prepared through the use of uniform sulfoselenide precursor solution. The structural integrity and quality of synthesized nanoparticles was analyzed via X-ray diffraction and Raman spectroscopy. The Uniformity of diffraction peaks in XRD coupled with lack of major binary or ternary phases in Raman suggest the successful synthesis of $Cu_2ZnSn(S_xSe_{1-x})_4$ nanoparticles over a wide range of sulfur to selenium ratios.

A uniform sulfoselenide anion precursor was prepared in a similar method reported in literature.[73] The role of anion precursor preparation and injection route on final structure of synthesized nanoparticles was also investigated. Findings from the study revealed that a uniform, mixed chalcogen solution is needed to produce uniform phase nanoparticles. Synthesis of particles was carried through a hot-injection method described previously.[20] For this specific reaction system, balancing the incorporation of selenium and sulfur in final nanoparticles proved to be a challenge. In all cases investigated in this study, selenium incorporation into the final nanocrystals was found to dominate. In order address this, excess anions relative to cations were introduced into the reaction vessel. Even in 200% excess anion samples, and with S:Se ratio of 1:1 added, sulfur to selenium ratios of the final nanoparticles was found to be 0.42:0.58. In these reaction systems, sulfur has been reported to form $H_2S$.[74] We attribute the discrepancy in sulfur to selenium ratios to loss of sulfur in this form.

A separate study was done, in order to test relative reactivity of sulfur and selenium, as well as gain some insight into the growth mechanism of kesterite phase $Cu_2ZnSn(S_xSe_{1-x})_4$ nanoparticles. In this study, CZTS nanoparticles were prepared using standard synthesis process reported in literature.[20] Different concentration of selenium were added to the synthesized CZTS nanoparticles, and aliquots were taken at different times after injection of selenium to study the structural properties of the nanoparticles. For excess selenium injected (S:Se=1:2)Analysis of these aliquots in XRD indicated the formation of a small peak to the left of the major peak ((112),(204),(316)) for kesterite CZTS. As the reaction continues for 1 hour, the peak continues to grow into a distinct CZTSe phase. For reaction lasting 6 hours after injection of selenium, the CZTS peak in XRD diminishes as the CZTSe peak grows and becomes the dominant phase. Moreover, investigation of samples were a lower concentration of selenium (S:Se=1:1) was injected into CZTS nanoparticles suggests the formation of a $Cu_xSe$ phase shortly after injection. Contrary to what was observed for higher concentrations of selenium added, this phase does not grow, but rather merges with the major CZTS phase, possible existing as a binary impurity in the final nanoparticles. This important observation agrees with findings from in situ energy-dispersive X-ray diffraction of a CZTS film during an annealing process under selenium rich vapor.[76]

In the reverse experiment, where different concentrations of sulfur were injected into CZTSe nanoparticles, the CZTSe phase remained intact for all concentrations of sulfur and even for reaction times lasting 5 hours. This suggests that CZTSe phase is highly favored and stable in these reactions.

## 5.2 Recommendations for Future Work

Findings from this study indicate that anion precursor plays a major role in crystal structure and phase purity of final nanoparticles. A more systematic study of the chemical state of anion precursor solutions used in this study would be highly beneficial to understanding these systems. This will be achieved by analyzing the mixture using mass spectrometry as the main analytical tool. Mass spectrometry techniques such as Electrospray Ionization Mass Spectrometry (ESI-MS) provide soft ionization techniques which allows for the analysis of large molecules, up to 100 kDa, with little or no fragmentation i.e. keeping their original structures intact.

Preliminary study, discussed in Chapter 4, suggests that sulfur exists as an alkylammonium-sulfide complex; this is also suggested in sulfur reduction mechanisms reported in previous studies.[74] Further investigation needs to be conducted in order to determine any fundamental differences in the chemical structure and properties of sulfur prepared in the traditional route i.e. dissolved in oleylamine, and the new method of preparing sulfur reported in this paper i.e. dissolved in a mixture of amine and thiol. Similarly, the chemical state of the sulfur-selenium mixture also needs to be analyzed. Any insight into chemical structure and complexing mechanism of this solutions is crucial to determine properties such as reactivity, chemical stability and oxidation states, and to shed light on the reaction chemistry of colloidal synthesis processes.

# LIST OF REFERENCES

LIST OF REFERENCES

1. Shockley, W. & Queisser, H. J. Detailed Balance Limit of Efficiency of p-n Junction Solar Cells. *J. Appl. Phys.* **32,** 510 (1961).

2. Wadia, C., Alivisatos, a P. & Kammen, D. M. Materials availability expands the opportunity for large-scale photovoltaics deployment. *Environ. Sci. Technol.* **43,** 2072–7 (2009).

3. Adams, W. G. & Day, R. E. The Action of Light on Selenium. *Philos. Trans. R. Soc. London* **167,** 313–349 (1877).

4. Ii, M. J. B., Mcbride, J. R. & Rosenthal, S. J. White-Light Emission from Magic-Sized Cadmium Selenide Nanocrystals. 15378–15379 (2005).

5. Wang, Q. & Webster, T. J. Nanostructured selenium for preventing biofilm formation on polycarbonate medical devices. *J. Biomed. Mater. Res. A* **100,** 3205–10 (2012).

6. Wang, W. *et al.* Device Characteristics of CZTSSe Thin-Film Solar Cells with 12.6% Efficiency. *Adv. Energy Mater.* n/a–n/a (2013). doi:10.1002/aenm.201301465

7. Brammertz, G. *et al.* Characterization of defects in 9.7% efficient Cu2ZnSnSe4-CdS-ZnO solar cells. *Appl. Phys. Lett.* **103,** 163904 (2013).

8. Chen, S., Gong, X. G., Walsh, A. & Wei, S.-H. Defect physics of the kesterite thin-film solar cell absorber Cu[sub 2]ZnSnS[sub 4]. *Appl. Phys. Lett.* **96,** 021902 (2010).

9. Chen, S., Yang, J.-H., Gong, X. G., Walsh, A. & Wei, S.-H. Intrinsic point defects and complexes in the quaternary kesterite semiconductor Cu_{2}ZnSnS_{4}. *Phys. Rev. B* **81,** 245204 (2010

10. Unold, T. & Schock, H. W. Nonconventional (Non-Silicon-Based) Photovoltaic Materials. *Annu. Rev. Mater. Res.* **41,** 297–321 (2011).

11. Scragg, J. J., Dale, P. J. & Peter, L. M. Synthesis and characterization of Cu2ZnSnS4 absorber layers by an electrodeposition-annealing route. *Thin Solid Films* **517,** 2481–2484 (2009).

12. Ennaoui, a. *et al.* Cu2ZnSnS4 thin film solar cells from electroplated precursors: Novel low-cost perspective. *Thin Solid Films* **517,** 2511–2514 (2009).

13. Bag, S. *et al.* Low band gap liquid-processed CZTSe solar cell with 10.1% efficiency. *Energy Environ. Sci.* **5,** 7060 (2012).

14. Todorov, T. K. *et al.* Beyond 11% Efficiency: Characteristics of State-of-the-Art Cu 2 ZnSn(S,Se) 4 Solar Cells. *Adv. Energy Mater.* **3,** 34–38 (2013).

15. Fischereder, A. *et al.* Investigation of Cu 2 ZnSnS 4 Formation from Metal Salts and Thioacetamide. *Chem. Mater.* **22,** 3399–3406 (2010).

16. Guo, Q., Hillhouse, H. W. & Agrawal, R. Synthesis of Cu 2 ZnSnS 4 Nanocrystal Ink and Its Use for Solar Cells. 11672–11673 (2009).

17. Guo, Q. *et al.* Fabrication of 7.2% efficient CZTSSe solar cells using CZTS nanocrystals. *J. Am. Chem. Soc.* **132,** 17384–6 (2010).

18. Guo, Q. *et al.* Enhancing the performance of CZTSSe solar cells with Ge alloying. *Sol. Energy Mater. Sol. Cells* **105,** 132–136 (2012).

19. Cao, Y. *et al.* High-efficiency solution-processed Cu2ZnSn(S,Se)4 thin-film solar cells prepared from binary and ternary nanoparticles. *J. Am. Chem. Soc.* **134,** 15644–7 (2012).

20. Miskin, C. K. *et al.* 9 . 0 % ef fi cient Cu 2 ZnSn ( S , Se ) 4 solar cells from selenized nanoparticle inks. **57,** 0–5 (2014).

21. Riha, S. C., Parkinson, B. a & Prieto, A. L. Solution-based synthesis and characterization of Cu2ZnSnS4 nanocrystals. *J. Am. Chem. Soc.* **131,** 12054–5 (2009).

22. Powalla, M. *et al.* High-efficiency Cu(In,Ga)Se2 cells and modules. *Sol. Energy Mater. Sol. Cells* (2013). doi:10.1016/j.solmat.2013.05.002

23. Redinger, A., Berg, D. M., Dale, P. J. & Siebentritt, S. The consequences of kesterite equilibria for efficient solar cells. *J. Am. Chem. Soc.* **133,** 3320–3 (2011).

24. Scragg, J., Ericson, T. & Kubart, T. Chemical insights into the instability of Cu2ZnSnS4 films during annealing. *Chem. Mater.* 4625–4633 (2011). at <http://pubs.acs.org/doi/abs/10.1021/cm202379s>

25. Wei, H. *et al.* Novel SnSxSe1−x nanocrystals with tunable band gap: experimental and first-principles calculations. *J. Mater. Chem.* **21,** 12605 (2011).

26. Shin, S. W. *et al.* A facile and low-cost synthesis of promising absorber materials on Cu2ZnSn(Sx,Se1−x)4 nanocrystals consisting of earth abundant elements with tunable band gap characteristics. *J. Mater. Chem.* **22,** 21727 (2012).

27. Ou, K.-L. *et al.* Hot-injection synthesis of monodispersed Cu2ZnSn(SxSe1−x)4 nanocrystals: tunable composition and optical properties. *J. Mater. Chem.* **22,** 14667 (2012).

28. Riha, S. C., Parkinson, B. A. & Prieto, A. L. Compositionally Tunable Cu2ZnSn(S1-xSex)4 Nanocrystals: Probing the Effect of Se-Inclusion in Mixed Chalcogenide Thin Films. 15272–15275 (2011).

29. Energy Crises (1970s). *History* at <1. http://www.history.com/topics/energy-crisis>

30. When Will We Run Out of Fossil Fuels. *EcoInfo* at <5. http://www.eco-info.net/fossil-fuel-depletion.html>

31. Annual Energy Review. *U.S. Environ. Prot. Agency* at <2. http://www.epa.gov/climatechange/ghgemissions/gases/co2.html>

32. Hansen, J., Sato, M. & Ruedy, R. Perception of climate change. *Proc. Natl. Acad. Sci. U. S. A.* **109,** E2415–23 (2012).

33. No Title. *World Bank* at <6. http://data.worldbank.org/indicator/NY.GDP.MKTP.KD.ZG>

34. NREL. *Basic Photovoltaic Principles and Methods*. (1982). at <http://medcontent.metapress.com/index/A65RM03P4874243N.pdf>

35. Singh, U. P. & Patra, S. P. Progress in Polycrystalline Thin-Film Cu(In,Ga)Se2 Solar Cells. *Int. J. Photoenergy* **2010,** 1–19 (2010).

36. Sah, C.-T., Noyce, R. N. & Shockleyt, W. Carrier Generation and Recombination in P-N Junctions and P-N Junction Characteristics. in *Preceedings IRE* **27,** 1228–1243 (1957).

37. Green, M. . *Solar cells: Operating principles, technology, and system applications*. (1982).

38. Yin, W.-J. *et al.* Engineering Grain Boundaries in Cu 2 ZnSnSe 4 for Better Cell Performance: A First-Principle Study. *Adv. Energy Mater.* n/a–n/a (2013). doi:10.1002/aenm.201300712

39. Fraas, L. & Partain, L. *Solar Cells and Their Applications-Second Edition*. (2010).

40. Miles, R. W., Zoppi, G. & Forbes, I. Inorganic photovoltaic cells. **10,** 20–27 (2007).

41. Wei, H., Guo, W., Sun, Y., Yang, Z. & Zhang, Y. Hot-injection synthesis and characterization of quaternary Cu2ZnSnSe4 nanocrystals. *Mater. Lett.* **64,** 1424–1426 (2010).

42. Adhi Wibowo, R., Hwa Jung, W. & Kim, K. H. Synthesis of Cu2ZnSnSe4 compound powders by solid state reaction using elemental powders. *J. Phys. Chem. Solids* **71,** 1702–1706 (2010).

43. Adhi Wibowo, R., Soo Lee, E., Munir, B. & Ho Kim, K. Pulsed laser deposition of quaternary Cu 2 ZnSnSe 4 thin films. *Phys. Status Solidi* **204,** 3373–3379 (2007).

44. Chen, S., Gong, X. G., Walsh, A. & Wei, S.-H. Crystal and electronic band structure of Cu2ZnSnX4(X=S and Se) photovoltaic absorbers: First-principles insights. *Appl. Phys. Lett.* **94,** 041903 (2009).

45. Li, J. V., Kuciauskas, D., Young, M. R. & Repins, I. L. Effects of sodium incorporation in Co-evaporated Cu2ZnSnSe4 thin-film solar cells. *Appl. Phys. Lett.* **102,** 163905 (2013).

46. Yin, W.-J., Wu, Y., Noufi, R., Al-Jassim, M. & Yan, Y. Defect segregation at grain boundary and its impact on photovoltaic performance of CuInSe2. *Appl. Phys. Lett.* **102,** 193905 (2013).

47. Yan, Y. *et al.* Electrically Benign Behavior of Grain Boundaries in Polycrystalline CuInSe2 Films. *Phys. Rev. Lett.* **99,** 235504 (2007).

48. Persson, C. & Zunger, A. Anomalous Grain Boundary Physics in Polycrystalline CuInSe2: The Existence of a Hole Barrier. *Phys. Rev. Lett.* **91,** 266401 (2003).

49. Shi, C., Shi, G., Chen, Z., Yang, P. & Yao, M. Deposition of Cu2ZnSnS4 thin films by vacuum thermal evaporation from single quaternary compound source. *Mater. Lett.* **73,** 89–91 (2012).

50. Daranfed, W., Aida, M. S., Attaf, N., Bougdira, J. & Rinnert, H. Cu2ZnSnS4 thin films deposition by ultrasonic spray pyrolysis. *J. Alloys Compd.* **542,** 22–27 (2012).

51. Ilari, G. M. *et al.* Solar Cell Absorbers Spin-Coated From Amine-Containing Ether Solutions. *Sol. Energy Mater. Sol. Cells* **104,** 125–130 (2012).

52. Juškėnas, R. *et al.* A two-step approach for electrochemical deposition of Cu–Zn–Sn and Se precursors for CZTSe solar cells. *Sol. Energy Mater. Sol. Cells* **101,** 277–282 (2012).

53. Mitzi, D. B., Gunawan, O., Todorov, T. K., Wang, K. & Guha, S. The path towards a high-performance solution-processed kesterite solar cell. *Sol. Energy Mater. Sol. Cells* **95,** 1421–1436 (2011).

54. Todorov, T. K., Reuter, K. B. & Mitzi, D. B. High-efficiency solar cell with Earth-abundant liquid-processed absorber. *Adv. Mater.* **22,** E156–9 (2010).

55. Hillhouse, H. W. & Beard, M. C. Solar cells from colloidal nanocrystals: Fundamentals, materials, devices, and economics. *Curr. Opin. Colloid Interface Sci.* **14,** 245–259 (2009).

56. De Mello Donegá, C., Liljeroth, P. & Vanmaekelbergh, D. Physicochemical evaluation of the hot-injection method, a synthesis route for monodisperse nanocrystals. *Small* **1,** 1152–62 (2005).

57. Alloyeau, D., Oikawa, T., Nelayah, J., Wang, G. & Ricolleau, C. Following Ostwald ripening in nanoalloys by high-resolution imaging with single-atom chemical sensitivity. *Appl. Phys. Lett.* **101,** 121920 (2012).

58. Werz, T., Baumann, M., Wolfram, U. & Krill, C. E. Particle tracking during Ostwald ripening using time-resolved laboratory X-ray microtomography. *Mater. Charact.* **90,** 185–195 (2014).

59. Sahu, P. & Prasad, B. L. V. Fine control of nanoparticle sizes and size distributions: temperature and ligand effects on the digestive ripening process. *Nanoscale* **5,** 1768–71 (2013).

60. Abe, S., Capek, R. K., De Geyter, B. & Hens, Z. Reaction chemistry/nanocrystal property relations in the hot injection synthesis, the role of the solute solubility. *ACS Nano* **7,** 943–9 (2013).

61. Murray, C. B., Norris, D. J. & Bawendi, M. G. Synthesis and characterization of nearly monodisperse CdE (E=sulfur, selenium, tellurium ) semiconductor nanocrystallites. *J. Am. Chem. Soc.* **115,** 8706–8715 (1993).

62. Li, H., Kanaras, A. G. & Manna, L. Colloidal branched semiconductor nanocrystals: state of the art and perspectives. *Acc. Chem. Res.* **46,** 1387–96 (2013).

63. Zamani, R. R. *et al.* Polarity-driven polytypic branching in cu-based quaternary chalcogenide nanostructures. *ACS Nano* **8,** 2290–301 (2014).

64. Li, W. *et al.* Morphology evolution of Cu(2-x)S nanoparticles: from spheres to dodecahedrons. *Chem. Commun. (Camb).* **47,** 10332–4 (2011).

65. Shao, X., Agarwal, A., Rajian, J. R., Kotov, N. a & Wang, X. Synthesis and bioevaluation of $^{125}$I-labeled gold nanorods. *Nanotechnology* **22,** 135102 (2011).

66. Protière, M., Nerambourg, N., Renard, O. & Reiss, P. Rational design of the gram-scale synthesis of nearly monodisperse semiconductor nanocrystals. *Nanoscale Res. Lett.* **6,** 472 (2011).

67. Battaglia, D. & Peng, X. Formation of High Quality InP and InAs Nanocrystals in a Noncoordinating Solvent. *Nano Lett.* **2,** 1027–1030 (2002).

68. Dai, Q. *et al.* Ligand Effects on Synthesis and Post-Synthetic Stability of PbSe Nanocrystals. *J. Phys. Chem. C* **114,** 16160–16167 (2010).

69. Tang, J. *et al.* Colloidal-quantum-dot photovoltaics using atomic-ligand passivation. *Nat. Mater.* **10,** 765–71 (2011).

70. Wang, J.-J., Liu, P., Seaton, C. C. & Ryan, K. M. Complete Colloidal Synthesis of Cu2SnSe3 Nanocrystals with Crystal Phase and Shape Control. *J. Am. Chem. Soc.* (2014). doi:10.1021/ja501591n

71. Siebentritt, S. & Schorr, S. Kesterites — a challenging material for solar cells. *Prog. Photooltaics Res. Appl.* (2012). doi:10.1002/pip

72. Liu, Y. *et al.* Alkylthiol-enabled Se powder dissolution in oleylamine at room temperature for the phosphine-free synthesis of copper-based quaternary selenide nanocrystals. *J. Am. Chem. Soc.* **134,** 7207–10 (2012).

73. Manuscript, A. ChemComm. (2014). doi:10.1039/C4CC02379J

74. Thomson, J. W., Nagashima, K., Macdonald, P. M. & Ozin, G. a. From sulfur-amine solutions to metal sulfide nanocrystals: peering into the oleylamine-sulfur black box. *J. Am. Chem. Soc.* **133,** 5036–41 (2011).

75. Wei, H. *et al.* Tunable band gap Cu2ZnSnS4xSe4(1−x) nanocrystals: experimental and first-principles calculations. *CrystEngComm* **13,** 2222 (2011).

76. Mainz, R. *et al.* Real-time observation of Cu2ZnSn(S,Se)4 solar cell absorber layer formation from nanoparticle precursors. *Phys. Chem. Chem. Phys.* **15,** 18281–9 (2013).

# APPENDICES

# Appendix A XRD

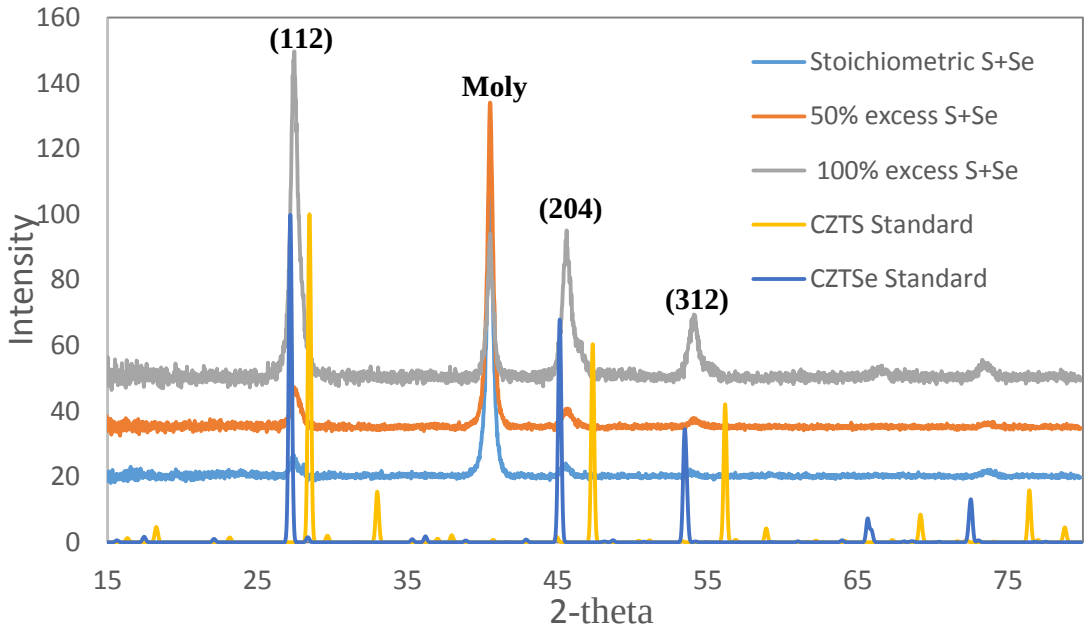


Figure A.1 XRD Spectra of CZTSSe nanoparticles prepared with S:Se ratio of 1:3.

It can be noted that there is little or no phase segregation in the particles due to singularity of peaks. There is a shift of peaks towards higher diffraction angle with excess amount of anion solution added.

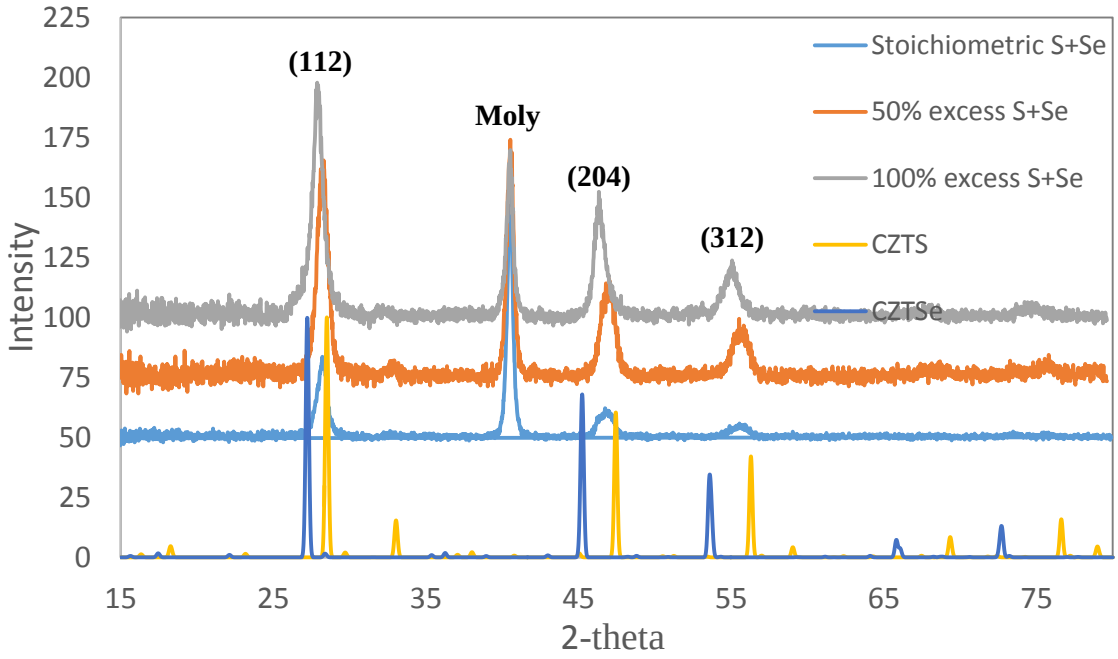


Figure A.2 XRD Spectra of CZTSSe nanoparticles prepared with S:Se ratio of 3:1.

There is little or no phase segregation in the particles due to singularity of peaks. There is a shift of peaks towards lower diffraction angle with excess amount of anion solution added as the selenium atoms replace sulfur.

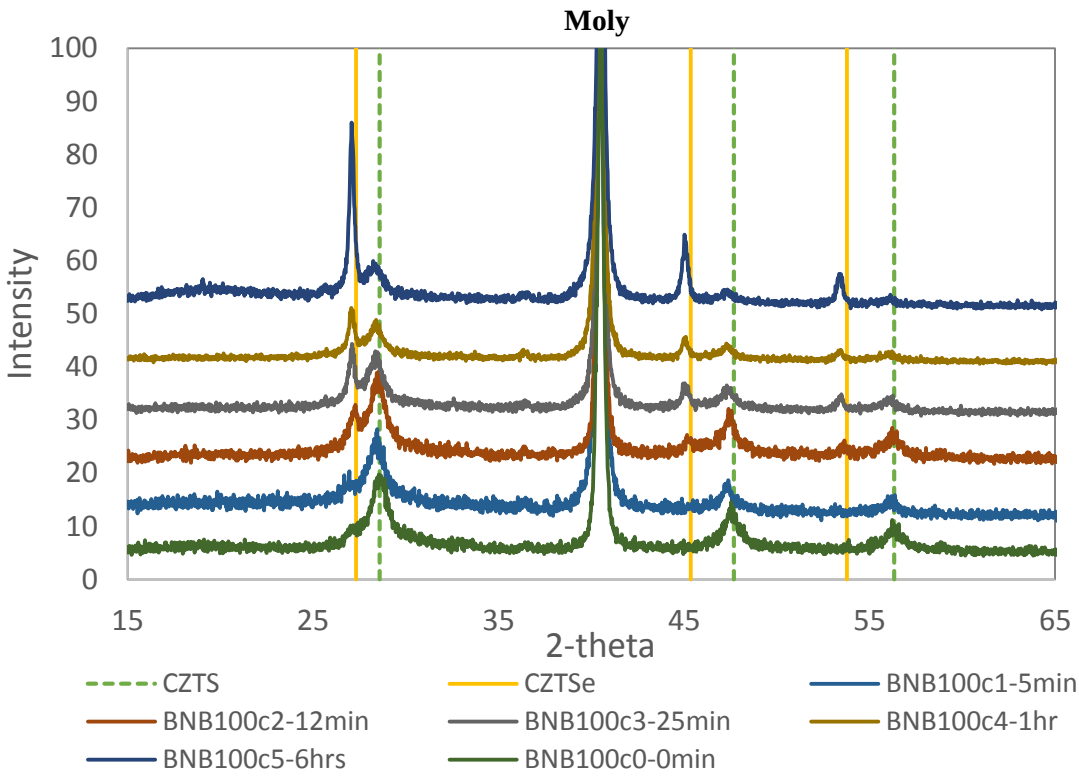


Figure A.3 XRD spectra of CZTS nanoparticles at different stages of structural evolution after excess selenium injection (S:Se=1:1.33)

The shoulder on the (112) peak at t=0 may be a result of lattice disorder and has been observed in CZTS particles in the past.

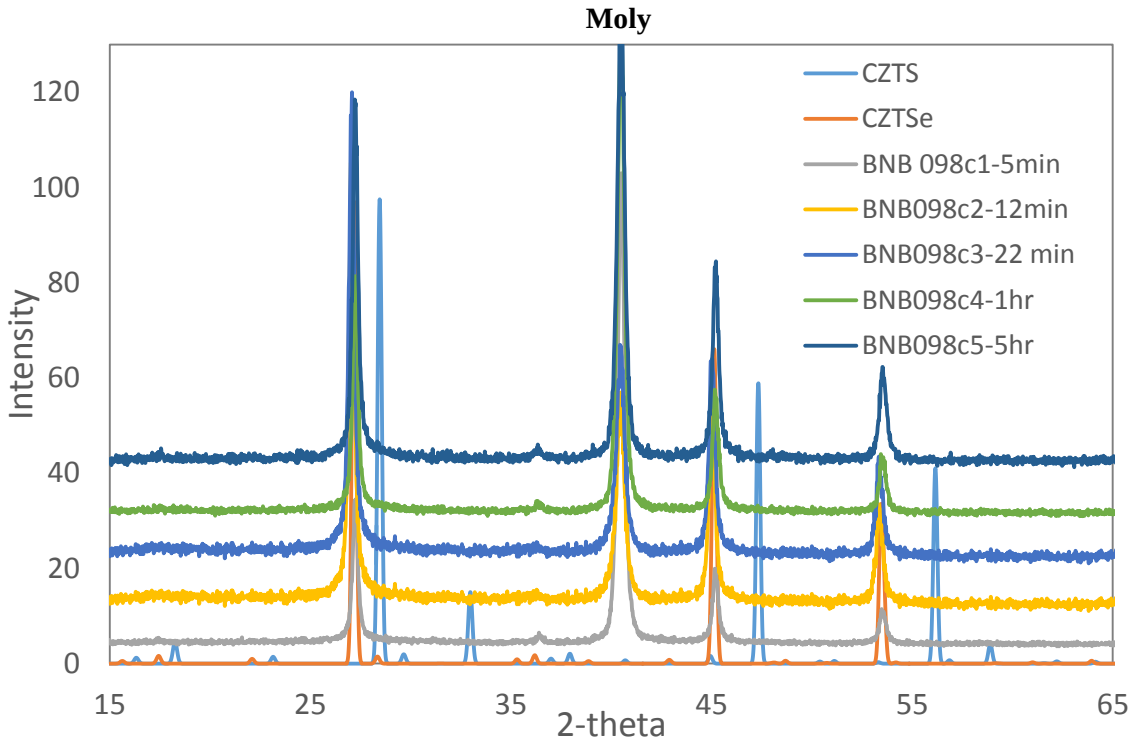


Figure A.4 XRD spectra of CZTSe nanoparticles hot-injected into a sulfur rich solution (S:Se=2:1).

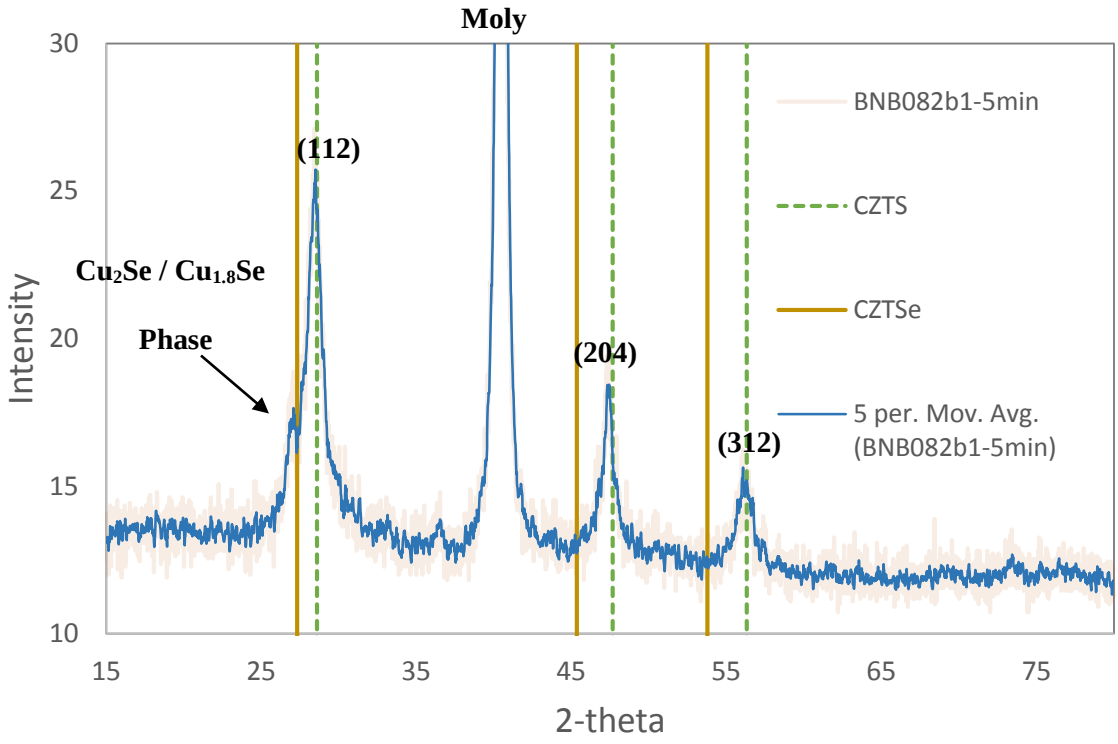


Figure A.5 XRD spectra of CZTS nanoparticles 5 min after selenium injection; (S:Se=1:1).

# Appendix B Raman

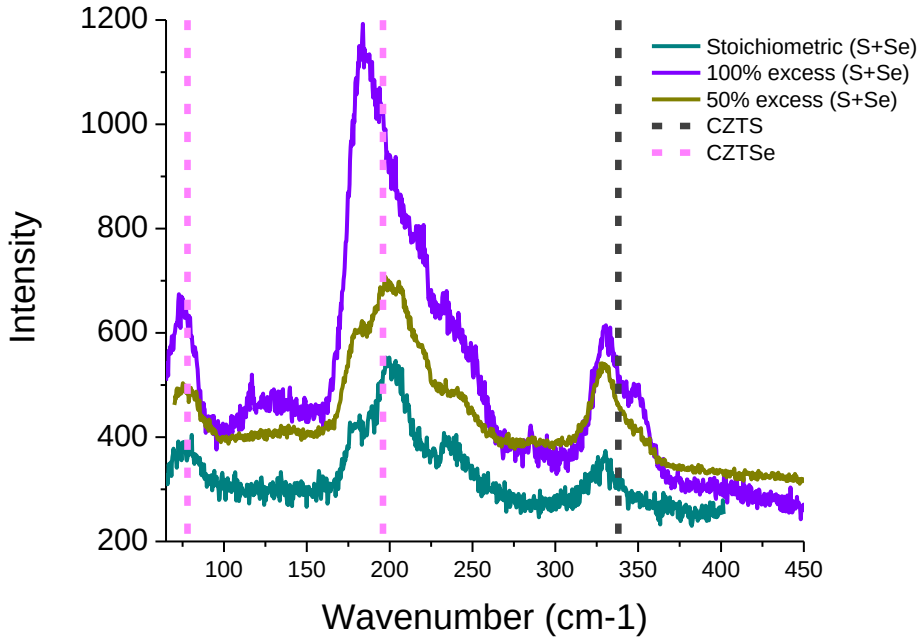


Figure B.1 Raman spectra of CZTSSe nanoparticles prepared with S:Se ratio of 1:3 and plotted for different amounts of excess anion(S+Se) solution added.

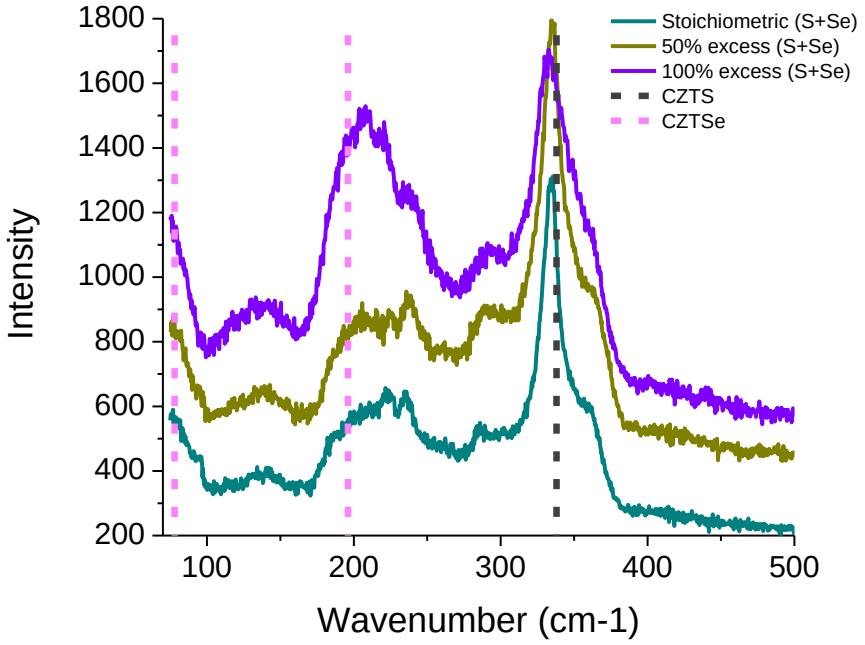


Figure B.2 Raman spectra of CZTSSe nanoparticles prepared with S:Se ratio of 3:1 and plotted for different amounts of excess anion (S+Se) solution added.